# Determination of stress orientation and magnitude in deep wells

M.D. Zoback[a],*, C.A. Barton[b], M. Brudy[b], D.A. Castillo[b], T. Finkbeiner[b], B.R. Grollimund[b], D.B. Moos[b], P. Peska[b], C.D. Ward[b], D.J. Wiprut[b]

[a] Department of Geophysics, Stanford University, Stanford, CA 94605-2215, USA
[b] GeoMechanics International, Palo Alto, CA, USA

Accepted 11 July 2003

### Abstract

In this paper, we review a suite of techniques for determination of in situ stress orientation and magnitude in deep wells and boreholes. As these techniques can be utilized in both vertical and highly deviated wells, they have had extensive application in the petroleum industry where knowledge of stress orientation and magnitude at depth is important for addressing a wide range of problems. The techniques we have developed for estimation of the maximum horizontal principal stress, $S_{Hmax}$, make extensive use of observations of non-catastrophic failures of the wellbore wall—both compressive failures (breakouts) and tensile failures (drilling-induced tensile fractures) as well as the stress perturbations associated with slip on faults cutting through the wellbore. The widespread use of wellbore imaging in the petroleum industry has been a critical development that makes utilization of these techniques possible. In addition to reviewing the theoretical basis for these techniques, we present case studies derived from oil and gas fields in different parts of the world. These case studies document the facts that the techniques described here yield (i) consistent stress orientations and magnitudes over appreciable depth ranges within and between wells in a given field (thus indicating that the techniques are independent of formation properties), (ii) stress magnitudes that are consistent with absolute and relative stress magnitudes predicted by Anderson and Coulomb faulting theories, (iii) stress orientations and relative magnitudes that are consistent with regional stress indicators and tectonics observed with other techniques at much larger scales and (iv) sufficiently well-constrained estimates of the full stress tensor that are useful in application to engineering problems such as wellbore stability.
© 2003 Elsevier Ltd. All rights reserved.

## 1. Introduction

Knowledge of stress magnitudes and orientation at great depth is of appreciable interest in both the geologic sciences and engineering. One of the most important uses of in situ stress data in the petroleum industry is associated with problems of wellbore instability. Arriving at practical engineering solutions to such problems (determination of optimal mud weights, stable trajectories, casing set points, etc.) requires accurate knowledge of the stress state at depth [1]. Because making stress measurements at great depth offers a unique set of challenges, we review in this paper techniques we have developed over the past 15 years that have proven to be especially efficacious in deep oil and gas wells. Ideally,

having a comprehensive geomechanical model of the subsurface would allow us to address a broad suite of problems ranging from wellbore stability during drilling, to determination of formation stability during production and from the selection of appropriate wellbore completion methods to the prediction of the long-term response of a reservoir to depletion. Needless to say, knowledge of the orientation and magnitude of the principal stresses is essential in any comprehensive geomechanical model. It has long been recognized that the maximum horizontal principal stress, $S_{Hmax}$, is the most difficult component of the stress tensor to accurately estimate. However, the widespread use of wellbore imaging devices has been an important development in the petroleum industry that has made application of the techniques described below possible. Ultrasonic borehole televiewers [2] and electrical imaging devices [3] yield detailed information about wellbore failure that is critically important in assessing stress

*Corresponding author. Tel.: +1-650-725-9295; fax: +1-650-725-7344.
E-mail address: zoback@pangea.stanford.edu (M.D. Zoback).

orientation and magnitude at depth. Because a well concentrates in situ stress in a mathematically known way, it is possible to obtain information about both stress orientation and magnitude from knowledge of the nature of wellbore failure (i.e., the presence, or absence, of compressional and tensile failures) and of how the well was drilled. Analysis of data obtained from multiple wells (and different stratigraphic levels in each) allows a fairly comprehensive model of the stress field to be developed. While such models are only accurate within certain limits (obviously, the more information used to derive a stress model at depth, the better the model is likely to be) the way in which uncertainties in stress estimates affect wellbore stability calculations can be addressed using rigorous, probabilistic methods [4,5].

Although stress is a tensor with six independent components, we will assume that the three principal stresses at depth are the vertical stress, $S_v$, and two horizontal principal stresses, $S_{Hmax}$ and $S_{hmin}$. While this can be shown to be the case in most places around the world (e.g., [6–10]), such a simplification will obviously be incorrect in some cases. For example, one would expect the orientation of principal stresses to be affected by topography in the shallow subsurface. Alternatively, as salt bodies at depth could introduce boundaries with near-zero shear strength at an arbitrary orientation, their presence would result in one principal stresses being normal to the boundary. Nonetheless, even when the principal stresses are not in horizontal and vertical planes, many of the principles described below that utilize observations of wellbore failure (in combination with independent knowledge of the least principal stress and overburden), can be quite helpful in constraining possible stress orientations and magnitudes.

In the sections that follow, we first introduce the concept of the frictional strength of the earth's crust in order to establish constraints on stress magnitudes as a function of depth and pore pressure. We then discuss practical aspects of determining the magnitude of $S_v$ from density measurements as well as the magnitude of the least principal stress, $S_3$ (which is usually $S_{hmin}$) from hydraulic fracturing data, leak-off tests (LOTs) and pressure while drilling (PWD) observations. While some of these techniques are relatively well known, they are discussed here both for completeness and because we use knowledge of the vertical and least principal stress to estimate the magnitude and orientation of the maximum principal stress. We first consider compressive and tensile wellbore failures in vertical wells and discuss how such observations allow us to determine the orientation and magnitude of $S_{Hmax}$. We then generalize this discussion and consider several techniques for determination of the magnitude of the maximum horizontal principal stress in arbitrarily deviated wells.

## 2. Stress magnitudes at depth and frictional faulting theory

It is helpful to consider the magnitudes of the greatest, intermediate, and least principal stresses at depths $S_1$, $S_2$, and $S_3$ in terms of $S_v$, $S_{Hmax}$ and $S_{hmin}$ in the manner originally proposed by Anderson [11]. In normal (N) faulting regions ($S_1 \equiv S_v$), gravity drives N faulting and fault slip occurs when the least horizontal principal stress ($S_{hmin}$) reaches a sufficiently low value depending on the depth and pore pressure ($S_v \geqslant S_{Hmax} \geqslant S_{hmin}$). When the stress field is very compressive, both horizontal stresses exceed the vertical stress ($S_3 \equiv S_v$), and folding and reverse faulting (RF) could occur when the maximum horizontal principal stress ($S_{Hmax}$) is sufficiently large relative to the vertical stress ($S_{Hmax} \geqslant S_{hmin} \geqslant S_v$). Strike-slip (SS) faulting represents an intermediate stress state ($S_2 \equiv S_v$), in which $S_{Hmax} \geqslant S_v \geqslant S_{hmin}$. In this case, faulting occurs when the difference between $S_{Hmax}$ and $S_{hmin}$ is sufficiently large.

Fig. 1 schematically demonstrates possible stress magnitudes for N, SS and RF environments when pore pressure ($P_p$) is hydrostatic (a–c) and when pore pressure approaches lithostatic (overburden) values at depth (d–f). At each depth, the range of possible values of $S_{hmin}$ and $S_{Hmax}$ are defined by Anderson faulting theory (which defines the relative stress magnitudes) and limited by Coulomb faulting theory (which determines maximum values of the differences between the maximum and minimum principal stresses in terms of the frictional strength of faulted rock at a given depth and pore pressure). Severely overpressured formations (Figs. 1d–f) are characterized by relatively small stress differences. In N and SS faulting domains, $S_{hmin}$, the least principal stress, must increase as $P_p$ increases. In SS and RF regimes, the maximum principal stress, $S_{Hmax}$, is severely reduced by high pore pressure. Thus, when pore pressure is very close to the vertical stress, both horizontal stresses must also be close to the vertical stress, regardless of whether it is an N, SS or RF environment.

Because the Earth's crust contains widely distributed faults, fractures, and planar discontinuities at many different scales and orientations, stress magnitudes at depth (specifically, the differences in magnitude between the maximum and minimum principal stresses) are limited by the frictional strength of these planar discontinuities. Although there are many observations around the world that stress magnitudes in the crust and are in equilibrium with its frictional strength (e.g., see reviews by Zoback and Healy [12] and Townend and Zoback [13]), we will not assume that this is always the case. Rather, we will consider the more general situation in which the stresses in the earth cannot be such that they exceed the frictional strength of pre-existing faults.
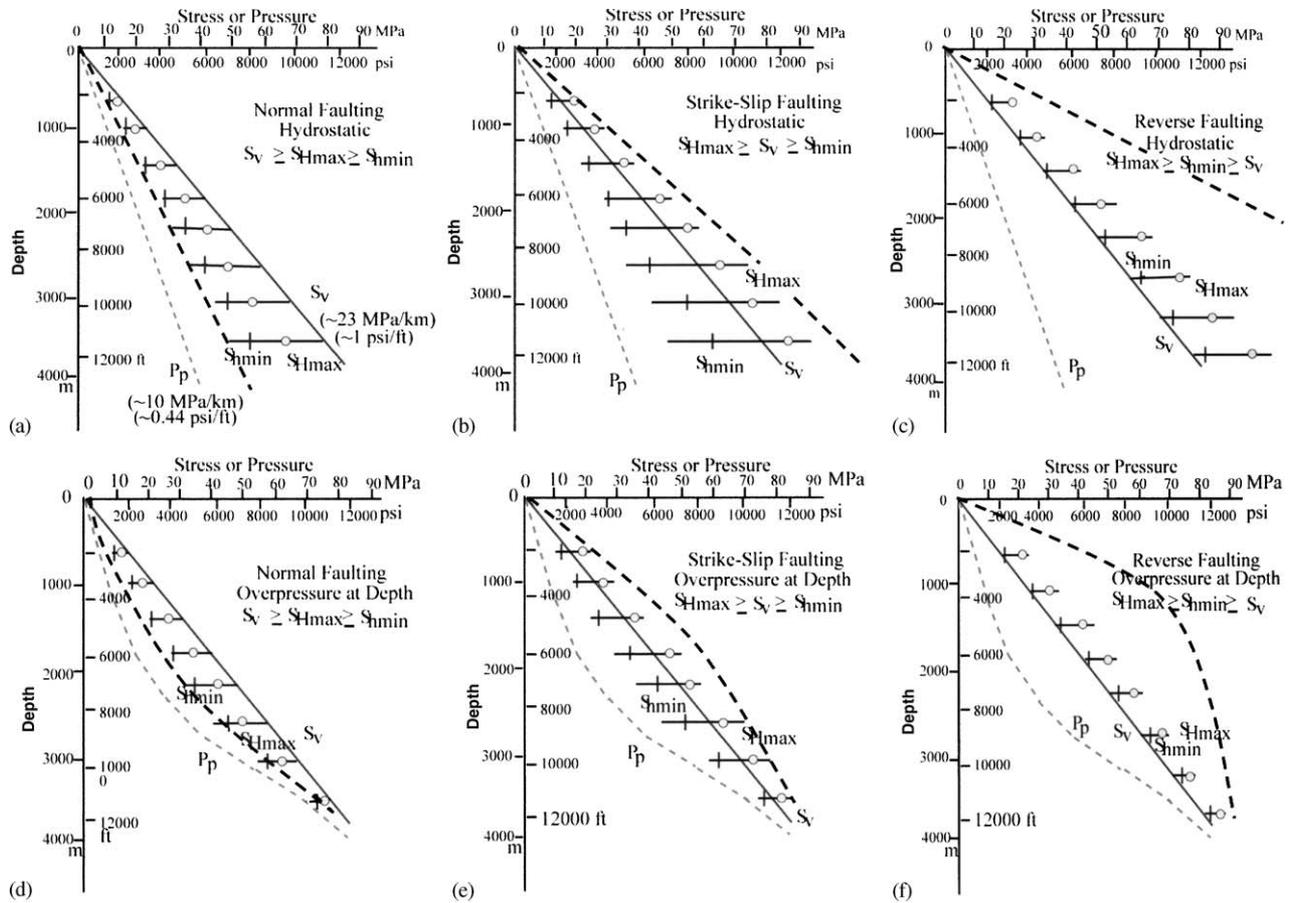
Fig. 1. Variation of stress magnitudes with depth in N, SS and RF stress regimes for hydrostatic (a–c) and overpressure conditions (d–f). Note that the difference between principal stresses increases with depth (due to the increase of crustal strength with depth but decreases as severe overpressure develops due to the decrease of crustal strength with elevated pore pressure. The heavy dashed lines indicate the limiting case for stress magnitudes based on frictional faulting theory based on Eqs. (2)–(4). Note that in cases of severe overpressure, there are very small differences between the three principal stresses, regardless of whether it is an N, SS or RF region.

Assuming that in any significant crustal volume, there are critically oriented faults that constrain stress magnitudes, Jaeger and Cook [14] showed that the limiting ratio of maximum principal effective stress $\sigma_1 \equiv (S_1 - P_p)$ and minimum principal effective stress at depth, $\sigma_3 \equiv (S_3 - P_p)$ is given by

$$\sigma_1/\sigma_3 = (S_1 - P_p)/(S_3 - P_p)$$
$$= [(\mu^2 + 1)^{1/2} + \mu]^2. \qquad (1)$$

To predict limiting stress differences at depth using this equation (i.e., the stress difference at which the shear stress will exceed the effective normal stress times the coefficient of friction, $\mu$), one must use Anderson's faulting theory to determine which of the principal stresses (i.e., $S_{Hmax}$, $S_{hmin}$, or $S_v$) correspond to $S_1$, $S_2$ and $S_3$. This will depend, on whether it is an N, SS, or RF environment. That is,

Normal faulting

$$\frac{\sigma_1}{\sigma_3} = \frac{S_v - P_p}{S_{hmin} - P_p} \leqslant [(\mu^2 + 1)^{1/2} + \mu]^2, \qquad (2)$$

Strike slip faulting

$$\frac{\sigma_1}{\sigma_3} = \frac{S_{Hmax} - P_p}{S_{hmin} - P_p} \leqslant [(\mu^2 + 1)^{1/2} + \mu]^2, \qquad (3)$$

Reverse faulting

$$\frac{\sigma_1}{\sigma_3} = \frac{S_{Hmax} - P_p}{S_v - P_p} \leqslant [(\mu^2 + 1)^{1/2} + \mu]^2. \qquad (4)$$

It is obvious from these equations that the maximum difference in principal stress magnitudes will depend on depth (as given by $S_v$), pore pressure, and knowing whether one is in an N, SS, or RF environment. This is illustrated in Fig. 1, where the heavy dashed lines in each figure indicate the limiting value of the principal stress differences at depth for either hydrostatic or over-pressure conditions. A coefficient of friction of 0.6 is used for illustration. Coefficients of friction between 0.6 and 1.0 have been shown to be applicable to the crust through laboratory studies on a wide range of rocks [15] and in situ experimentation in N, SS and RF environments [12,13,16]. It should be noted that this discussion neglects the cohesive strength of faults [14]. At

significant depth, the effect of incorporating the cohesive strength of a fault is relatively unimportant in terms of the stress magnitudes predicted by Eqs. (2)–(4). At shallower depth, e.g., in civil engineering and mining applications, this may not be true.

Given that stress in the crust is limited by the frictional strength of faults, it is straightforward to estimate the range of possible stress states at any given depth and pore pressure. Fig. 2 illustrates the range of allowable values for horizontal principal stresses in the earth's crust for N, SS and RF environments using Coulomb faulting theory and Anderson's stress and faulting classification system. Such figures delineate the range of possible stress magnitudes at a particular depth and pore pressure for a particular coefficient of friction (again taken to be 0.6). Fig. 2 is computed for a depth of 3 km (assuming an average overburden density of 2.3 gm/cm$^3$, appropriate for sedimentary rocks) for hydrostatic pore pressure (Fig. 2a) and for significant overpressure (Fig. 2b). The construction of such figures is discussed by Zoback et al. [17] and Moos and Zoback



Fig. 2. Stress polygons that define possible magnitudes of $S_{hmin}$ and $S_{Hmax}$ at any given depth as defined by Anderson's faulting theory and Coulomb faulting theory for a given coefficient of friction and pore pressure. The circumference of the polygon corresponds to a case of active faulting (see inset of upper figure). The upper figure illustrates the size of the polygon for hydrostatic pore pressure and the lower figure illustrates what happens when pore pressure is equal to 80% of the overburden. As shown in Fig. 1, there is appreciably less stress anisotropy at depth when pore pressure is high.

[18]. Briefly, $S_{Hmax} \geqslant S_{hmin}$ requires all stress states to be above the diagonal line of unit slope. The vertical and horizontal lines intersecting at $S_{Hmax} = S_{hmin} = S_v$ separate the stress fields associated with N, SS and RF faulting stress environments as defined by Anderson. The vertical line in the lower left of the polygon indicates the lowest value of $S_{hmin}$ possible in an N faulting environment as predicted using Eq. (2). In other words, for the value of $S_{hmin}$ shown by this line, a Mohr circle would exactly touch a frictional failure envelope with a slope of 0.6. Similarly, the horizontal line defining the top of the polygon corresponds to the value of $S_{Hmax}$ at which RF would occur. The diagonal line bounding the polygon on the upper left corresponds to the value of $S_{Hmax}$ at which SS faulting would occur for a given value of $S_{hmin}$. Thus, in every case, the stress at depth must be somewhere within the stress polygon. If the state of stress is in frictional failure equilibrium, it falls on the outer periphery of the polygon, depending, of course, on whether the stress state is N, SS or RF (inset).

Fig. 2b illustrates the fact that elevated pore pressure (80% of lithostatic) reduces the difference among principal stresses at depth as shown previously in Figs. 1d–f. When pore pressure is high, all three principal stresses must be much closer in magnitude to the vertical stress because of the reduced frictional strength of pre-existing faults. When pore pressure is very high, small stress differences are sufficient to cause faulting and relatively small changes in the stress field can cause a transition from one style of faulting to another. Whereas, when pore pressure is hydrostatic, large changes of the stress magnitudes must occur to go from an NF/SS faulting environment to an RF/SS environment.

The stress polygon shown in Fig. 2 permits a wide range of stress values at depth and would not seem to be of much practical use in limiting stress magnitudes at depth. However, as LOTs or hydraulic fracturing tests are often available at depth and provide a good estimate of the least principal stress, the polygon is useful for estimating the possible range of values of $S_{Hmax}$. Furthermore, we illustrate below that if one also has information about the existence of either compressive or tensile wellbore failures, one can often put narrower (and hence, more useful) bounds on possible stress states at depth. In other words, by combining the constraints on stress magnitudes obtained from the frictional strength of the crust, measurements of the least principal stress from LOTs and observations of wellbore failure, it is possible to place strong constraints on the in situ stress state [18].

## 3. Determination of $S_v$ from density measurements

Mathematically, the magnitude of $S_v$ can be calculated by integration of rock densities from the surface to

the depth of interest, $z$. In other words,

$$S_v = \int_0^z \rho(z)g\,\mathrm{d}z \approx \bar{\rho}gz, \qquad (5)$$

where $\rho(z)$ is the density as a function of depth, $g$ is the gravitational acceleration constant and $\bar{\rho}$ is mean overburden density. In offshore areas, we correct for water depth

$$S_v = \rho_w gz_w + \int_{z_w}^z \rho(z)g\,\mathrm{d}z \approx \rho_w gz_w + \bar{\rho}g(z - z_w), \qquad (6)$$

where $\rho_w$ is the density of water and $z_w$ is the water depth. As $\rho_w \sim 1\,\mathrm{gm/cm}^3$ (1.0 SG), water pressure (hydrostatic pressure) increases at a rate of 10 MPa/km (0.44 psi/ft). Most clastic sedimentary rocks have an average density of about $2.3\,\mathrm{g/cm}^3$ which corresponds to a porosity of about 15%. This results in a vertical principal stress that increases with depth at a rate of 23 MPa/km (or conveniently, $\sim 1\,\mathrm{psi/ft}$) as shown in Fig. 1 which would be applicable on land where Eq. (5) would be used. Stress measurements made at depth in highly compressional areas using the hydraulic fracturing techniques described below, confirm this (e.g., [19]).

Some of the practical problems associated with the computation of $S_v$ are illustrated in Fig. 3 for an offshore well. The density log was not recorded all the way to the sea bottom because it was not of geologic interest. However, density is quite low at the sea floor (porosity can exceed 60%) and rapidly increases with depth. Hence, the manner in which measured values are extrapolated to the surface is quite important. In addition, there is sometimes considerable scatter in the measured density values, especially when hole conditions are poor (Fig. 3a). In fact, when wellbores are significantly enlarged, the density values tend to be low. Hence, it is necessary to both edit and extrapolate the data in order to determine the vertical stress with depth as shown in Fig. 3b.

## 4. Determination of $S_3$ (usually $S_{hmin}$) using hydrofracs and leak-off tests

The next step in determining the magnitude of stresses at depth is the determination of the least principal stress, $S_3$, which corresponds to $S_{hmin}$ in N and SS faulting areas. This can be accomplished with considerable accuracy through hydraulic fracturing as Hubbert and Willis [20] presented a compelling argument that hydraulic fractures in the earth will always propagate perpendicular to the orientation of the least principal stress, $S_3$. That is, because the work done to open a fracture to a given amount is proportional to the product of the stress acting perpendicular to the fracture plane times the amount of opening, hydraulic fractures will always propagate perpendicular to the least



(a)



(b)
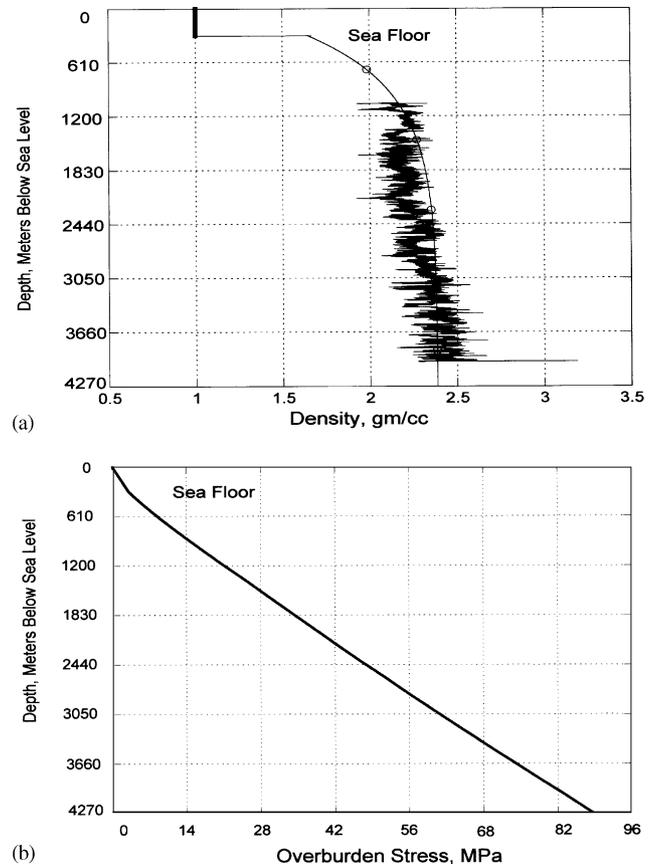
Fig. 3. Density log from an offshore well. (a) Density measurements were not made to the sea floor and need to be extrapolated from the depth of the shallowest measurement. Note too that the log is quite noisy, most likely due to hole rugosity (see text). (b) Overburden stress corresponding to extrapolated (and filtered) density log.

principal stress because it is the least energy configuration. Hubbert and Willis [20] confirmed this with simple sand-box laboratory tests and pointed out that the orientation of a hydraulic fracture is controlled by the orientation of the least principal stress and the pressure needed to propagate a hydraulic fracture is controlled by the magnitude of the least principal stress. While determination of the minimum stress through hydraulic fracturing has been widely discussed (e.g., [21]), we discuss below two aspects of the determination of $S_3$ that are specific to tests in deep wells when conventional hydrofrac tests are either not available, or are impossible due to drilling conditions.

A common type of test in the oil industry that yields important information about the least principal stress is called an LOT. LOTs are conducted after casing has been cemented in place and the casing shoe is drilled out a short distance (usually $\sim 5\,\mathrm{m}$). When such tests are carried out fully, they are referred to as extended leak-off tests (XLOTs). A schematic pressure–time history is shown in Fig. 4 (after Gaarenstroom et al. [22]) that illustrates many of the terms commonly associated with XLOTs. It should be noted that Fig. 4 represents
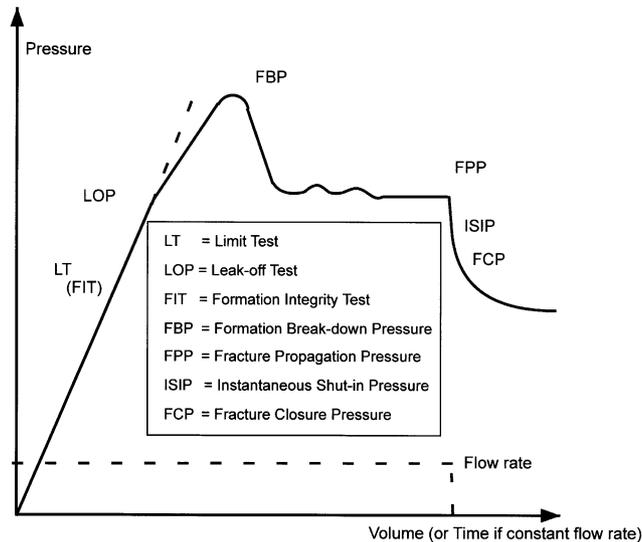
Fig. 4. Schematic illustration of an extended LOT (after Gaarenst-room et al. [22]). The various terms associated with such a test are explained in the text.

pressure at the surface during a minifrac or LOT (note that the pressure is zero at the beginning of the test). To determine the magnitude of the least principal stress at the depth of the test, it is necessary to add the pressure in the wellbore due to the column of wellbore fluid. In fact, it is always preferable to measure pressure downhole during such tests (see below).

If pumping into a well occurs at constant rate, the pressure should increase linearly with time (like a fluid in a container) as the volume of the system is fixed. At the pressure where there is a distinct departure from a linear increase of wellbore pressure with time (referred to as the LOP, the leak-off point) a hydraulic fracture must exist. The reason for this is that there cannot be a notable decrease in the rate of wellbore pressurization unless there is a significant increase in the system volume. In other words, the pressure in the wellbore must be sufficient to propagate the fracture far enough from the wellbore to increase the system volume at a rate that is large enough to affect the rate of wellbore pressurization. Thus, a hydraulic fracture propagating away from the wellbore, perpendicular to the least principal stress, must exist. A clear LOP (corresponding to a distinct break-in-slope) is approximately equal to the least principal stress (as shown) although the wellbore pressure may also reflect some near-wellbore resistance to fracture propagation associated with the near-wellbore stress concentration (see below).

If the LOP is not reached, a limit test, or formation integrity test (LT, or FIT), is said to have been conducted. Such tests merely indicate that at the maximum pressure achieved, the fluid did not propagate away from the wellbore wall. This is either because the maximum wellbore pressure was not sufficient to initiate

a fracture or, if a fracture was initiated, because this pressure did not exceed the least principal stress.

The peak pressure reached during a LOT or minifrac is termed the formation breakdown pressure (FBP) and represents the pressure at which unstable fracture propagation away from a wellbore occurs (fluid flows into the fracture from the wellbore faster than it does into the wellbore from the pump; hence the pressure drops in the wellbore). The difference between the LOP and FBP is a complex function of the stress concentration around a well and the conditions immediately surrounding the well (especially when a hydrofrac is being initiated through perforations). As pumping continues at constant rate, the pumping pressure measured in the well drops below the FBP to a relatively constant value called the fracture pumping pressure (FPP), the pressure associated with propagating the fracture far from the well. In the absence of appreciable near-wellbore resistance (i.e., if the flow rate and fluid viscosity are low enough), the FPP is close to the least principal stress (e.g., [23]). Hence, the FPP and LOP values should be similar. It should be noted that a distinct FBP need not be present in a reliable XLOT.

An even better measure of the least principal stress is obtained from the instantaneous shut-in pressure (ISIP) after abruptly stopping flow into the well, as any pressure gradient due to viscous pressure losses disappears [24] when pumping stops. In carefully conducted tests, constant (and low) flow rates of $\sim 150\,l/$min (1 BBL/min), or less, are maintained and low-viscosity fluid (such as water) is used and pressure is continuously measured. In such tests, the LOP, FPP, and ISIP often have approximately the same values and can provide redundant and reliable information about the magnitude of $S_3$. If a viscous frac fluid was used, or a frac fluid with suspended propant, FPP will increase due to large friction losses. In such cases the fracture closure pressure (FCP) is a better measure of the least principal stress than the FPP or ISIP. The FCP is determined by plotting pressure as a function of $\sqrt{\text{time}}$ after shut-in and detecting a change in linearity of the pressure decay [25]. However, if used inappropriately, FCPs can underestimate the least principal stress and care must be taken to ensure that this is not the case.

Fig. 5 shows a compilation of pore pressure and LOT data from the Visund field in the northern North Sea [26]. Pore pressure is hydrostatic to about 1500 m depth and then increases to approximately 75% of the vertical stress at greater depth. There are three important features to note about the least principal stress values at depth. First, the measurements are reasonably repeatable and consistent throughout the field. Second, the measurements clearly indicate a compressional stress state because even at relatively shallow depth (where pore pressure is hydrostatic), the magnitude of the least principal stress is close to the vertical stress. We show
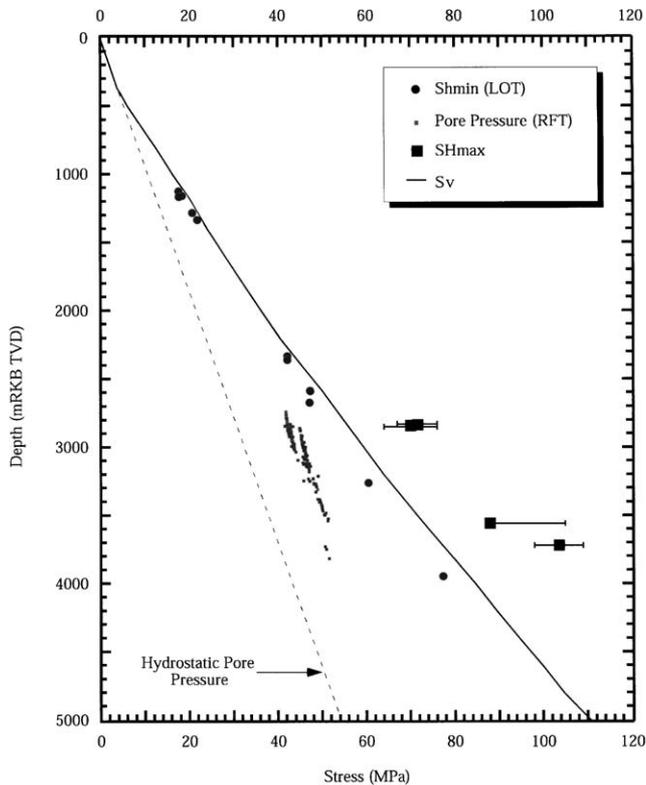
Fig. 5. Overburden stress from integration of density logs (solid block line), pore pressure measurements (small dots), $S_{hmin}$ values determined from LOTs in different wells (larger dots) and estimates of $S_{Hmax}$ (boxes and error bars) determined from analysis of drilling-induced tensile fractures in the Visund field of the northern North Sea (after Wiprut et al. [26]).

below that the magnitude of $S_{Hmax}$ is greater than $S_v$ such that an SS faulting regime exists in this region. However, because $S_{hmin}$ is close to $S_v$, if the magnitude of $S_v$ had been slightly under-estimated (due to uncertainties in density), or if $S_3$ was slightly higher than the values shown (because the measurements were not carefully conducted), it would appear as if $S_3 = S_v$ and a RF regime would have been indicated. While this distinction might seem to be relatively insignificant, if one were concerned with the propagation of hydraulic fractures to stimulate production in low-permeability reservoirs, if $S_3 = S_{hmin}$, vertical hydrofracs would propagate in the formation whereas if $S_3 = S_v$, horizontal fractures would form. This emphasizes the need both to accurately integrate density logs to minimize errors in $S_v$ and to carry out LOTs as carefully as possible to determine $S_{hmin}$ with as much confidence as possible. In fact, in the Visund field, considerable effort was taken to estimate rock density at shallow depth to derive the curve shown. Had this not been the case, it would have been difficult to determine whether the least principal stress was less than, or equal to, the vertical stress.

Unfortunately, in practice, many LOTs are conducted using poor field procedures. When interpreting such tests, two questions must be kept in mind in order to decide whether the test can be used to obtain a measure of the least principal stress. First, is there an indication that the LOP was reached? If so, the LOP can be considered an approximate measure of the least principal stress. If not, then the test must be considered a FIT and the maximum pressure achieved cannot be used to estimate the least principal stress. Second, was a stable FPP achieved? If so, the fracture propagated away from the well and the shut-in pressure is likely a good measure of $S_3$. While these two questions are straightforwardly answered when there is a good record of a test, it is sometimes necessary to rely on a single reported value, not knowing whether it refers to a reasonable estimate of the least principal stress. In fact, the pressure–time record is sometimes approximated by a few distinct data points obtained by reading pressure off a fluctuating dial gauge and estimating flow rate by counting pump strokes. In such cases, determination of an accurate least principal stress value from a LOT is essentially impossible. Values of LOTs that are markedly lower in the expected regional trend should also be treated with extreme caution as these tests may simply indicate a poor quality cement job rather than an anomalously low value of the least principal stress.

PWD is a pressure while drilling measurement that continually measures annular pressures during the drilling process [27] and has the potential for providing information about the magnitude of the least principal stress, especially in difficult drilling situations. This measurement is generally taken some 5–10 m behind the bit and allows for accurate downhole determination of mud weight, equivalent circulation density (ECD), swab and surge pressures. Pressure values are both transmitted to the surface in real time during drilling and recorded downhole in memory that is read when the bottom-hole assembly is brought to the surface. Fig. 6a shows a number of drilling-related parameters as a function of time (including PWD in the right column), that were measured during drilling operations. Note the step-like nature of the pressure drop that occurred when drilling was stopped to connect a section of drill pipe. When drilling resumed the pressure abruptly increased. This step in pressure allows us to define the difference between the ECD (the ECD which corresponds to the bottom-hole pressure during drilling) to the static mud weight. In this case, the viscous resistance to mud circulation during drilling results in a difference between the ECD and static mud weight of 0.33 PPG.

There are three ways that PWD data can be used to better constrain the minimum horizontal stress: improving the accuracy of LOT measurements, identifying lost circulation incidents and identifying *ballooning* incidents. With respect to LOTs, it is important to recognize that such tests are normally recorded at the surface and the pressure downhole is determined by adding a
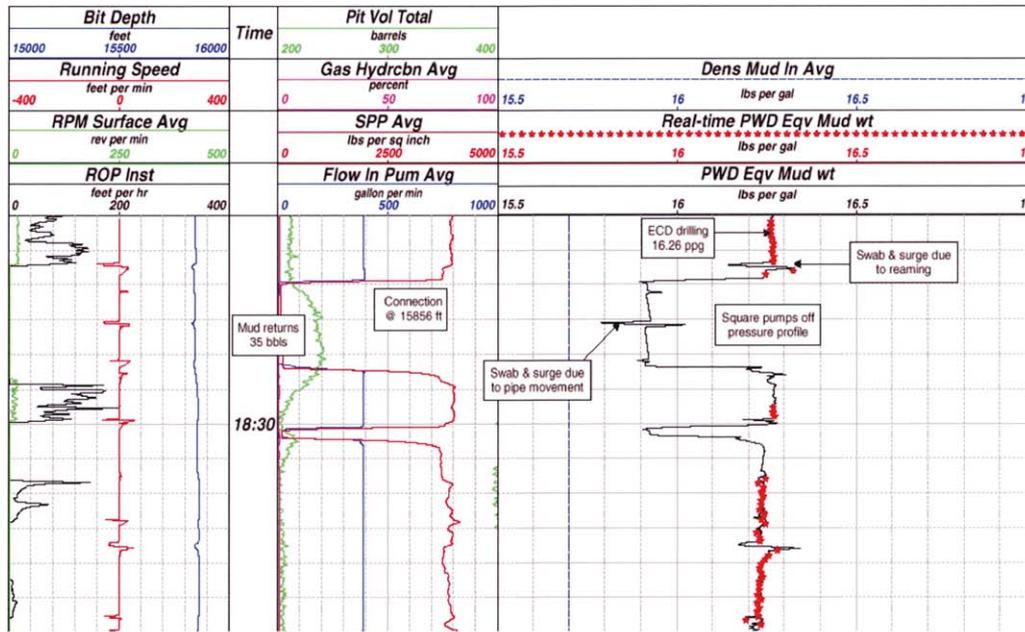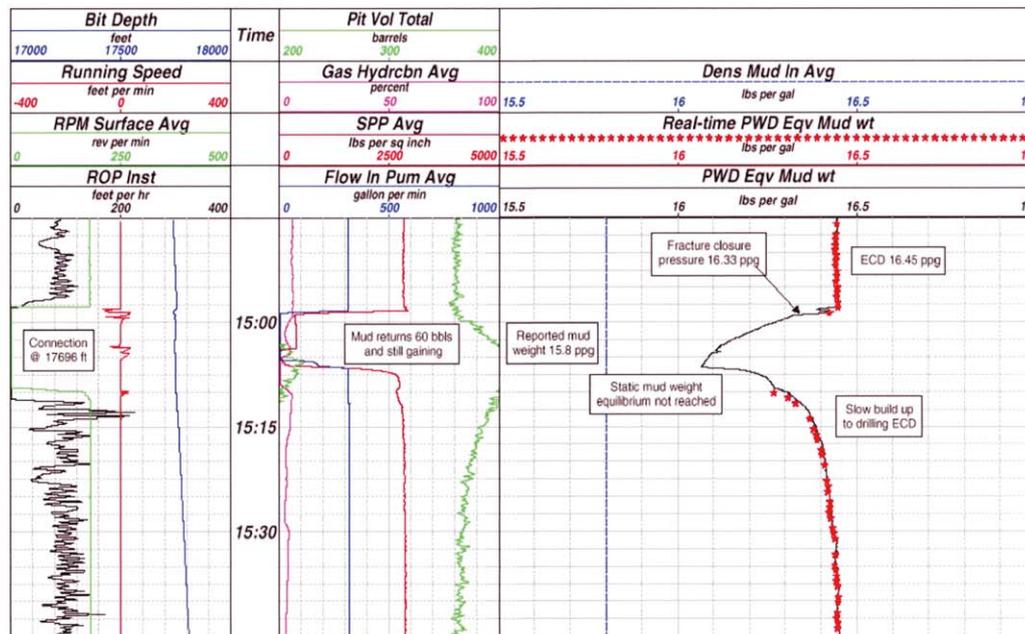
Fig. 6. PWD observations show in (a) a step-like change in pressure when drilling was stopped to connect a section of drill pipe. Note that the ECD is 0.33 PPG higher than the static mud weight. In contrast, note in (b) that when the pump is shut off for a connection the pressure slowly decays, then slowly builds up again when the pump is turned back on. This behavior is reminiscent of a balloon because it implies the storage of drilling fluid upon pressurization and the return of this fluid into the wellbore when the pumps are shut off.

pressure corresponding to the static mud column to the surface. PWD records pressure downhole directly and a number of comparisons have shown that there can be significant differences between downhole pressures calculated from surface measurements and actual downhole LOT measurements [28]. This difference could be caused by suspended solids, pressure and temperature effects on mud density, or measurement error. There is

an additional error during the pumping and shut-in phases that could be due to the mud gels, mud compressibility or pressure loss in the surface lines.

PWD also accurately measures the pressures imposed on the formation during a lost circulation incident [28]. There is often some uncertainty about exactly where the losses are happening in a long open hole section, so the PWD measurement may need to be referenced to

the appropriate depth. Sometimes repeated resistivity logs can help identify the depths at which the losses occur. Similar to what happens in a LOT, losses of drilling with mud occur at pressures slightly higher than the least principal horizontal stress. The accurate determination of such pressures with PWD data yield reliable estimates of the least principal stress because the fracture must be propagating into the far field away from the wellbore in order for circulation to be lost.

Finally, ballooning, sometimes called loss/gain or wellbore breathing, is now generally thought to be caused by the opening and closing of near-wellbore fractures [29] in deviated wells. While circulating with an ECD close to the least principal stress, small mud losses occur which, when the pumps are turned off, begin to bleed back into the wellbore. In Fig. 6a, we observe that the pressure drop from the ECD to the static mud weight is quite abrupt when the pump stops and then increases abruptly when drilling resumes. Note the markedly different behavior in Fig. 6b—when the pump is shut off for a connection, the pressure slowly decreases, then slowly builds up when the pump is turned back on. This behavior is reminiscent of a balloon because it implies the storage of drilling fluid upon pressurization and the return of this fluid into the wellbore when the pumps are shut off. Thus, the PWD signature during ballooning has a distinctive curved pressure profile (Fig. 6b) as closing fractures bleed fluid back into the wellbore and fractures are refilled as circulation is resumed. The ECD at which ballooning occurs can be used as a lower bound for the magnitude of the least principal stress (if $S_3$ was lower, lost circulation would have occurred). In fact, it has been argued [29] that unless the ECD was close to $S_3$, ballooning cannot occur. Modeling by Ito et al. [30] indicates that the most likely reason ballooning occurs is that en echelon tensile fracture forms in the wall of a deviated well (see below) that stores fluid at the pressure corresponding to the ECD during drilling. When the pump is shut off and the pressure drops to the static mud weight, the mud comes out of the fractures and back into the wellbore.

## 5. Wellbore failure and determination of stress orientation in vertical wells

For the case when $S_v$ is a principal stress, the effective stresses ($\sigma_{ij} = S_{ij} - \delta_{ij}P_p$) around a vertical wellbore of radius $R$ are described in terms of a cylindrical coordinate system through the well-known Kirsch equations [31] by the following:

$$\sigma_{rr} = \frac{1}{2}(S_{Hmax} - S_{hmin})\left(1 - \frac{R^2}{r^2}\right) + \frac{1}{2}(S_{Hmax} - S_{hmin})\left(1 - \frac{4R^2}{r^2} + \frac{3R^4}{r^4}\right)\cos 2\theta + \frac{\Delta P R^2}{r^2}, \quad (7)$$

$$\sigma_{\theta\theta} = \frac{1}{2}(S_{Hmax} - S_{hmin})\left(1 - \frac{R^2}{r^2}\right) - \frac{1}{2}(S_{Hmax} - S_{hmin})\left(1 - \frac{3R^4}{r^4}\right)\cos 2\theta + \frac{\Delta P R^2}{r^2} - \sigma^{\Delta T}, \quad (8)$$

$$\tau_{r\theta} = \frac{1}{2}(S_{Hmax} - S_{hmin})\left(1 + \frac{2R^2}{r^2} - \frac{3R^4}{r^4}\right)\sin 2\theta, \quad (9)$$

where $\theta$ is measured from the azimuth of $S_{hmin}$ and for simplicity we assume (for the moment) that the mud weight in the wellbore is equal to the pore pressure, $P_p$. $\sigma^{\Delta T}$ represents thermal stresses arising from the difference between the mud temperature and the formation temperature ($\Delta T$), as is discussed below. Note that the stress components described in these equations are independent of elastic moduli.

There are several important points about these equations that are illustrated in Fig. 7 for the following parameters: $S_{Hmax} = 90$ MPa (at N90°E); $S_v = 88.2$ MPa (depth 3213 m); $S_{hmin} = 51.5$ MPa and $P_p = P_{mud} = 31.5$ MPa. First, the stress concentration varies strongly as a function of both position around the wellbore and distance from the wellbore wall and is symmetric with respect to the direction of the horizontal principal stresses. As shown in Fig. 7a, $\sigma_{\theta\theta}$ (the so-called *hoop* stress) is strongly compressive at the azimuth of $S_{hmin}$ and decreases rapidly with distance from the wellbore wall as given by Eq. (8). Similarly, at the azimuth of $S_{Hmax}$, the hoop stress is quite low (approximately zero) because of the relatively large difference between $S_{Hmax}$ and $S_{hmin}$. Although, the hoop stress increases rapidly with distance from the wellbore wall, when $S_{Hmax}$ is appreciably larger than $S_{hmin}$ (see below), the wellbore wall itself can go into tension at the azimuth of $S_{Hmax}$ which leads to the formation of drilling-induced tensile wall fractures [18,32]. These only propagate an extremely small distance (mm to cm) from the wellbore wall [33], consistent with the rapid increase of hoop stress with radial distance from the wellbore wall. Tensile wall fractures are more likely to form when wellbore pressure is larger than the pore pressure and when the mud is much cooler than the formation temperature, as discussed further below.

In Fig. 7a, it is obvious that compressive failure of the wellbore wall is most likely to occur in the area of maximum compressive hoop stress (at the azimuth of $S_{hmin}$) if the stress concentration reaches the rock strength [34,35]. The zone of compressive failure around the well is shown in Fig. 7b assuming, for illustrative purposes, a Mohr–Coulomb failure criterion and $Co = 45$ MPa, $\mu_i = 1.0$. The colors in Fig. 7b indicate the value of rock strength required to prevent failure. Hence, hot colors means it takes high strength to prevent failure (because the stress concentration is so high) whereas cold colors mean that even a low-strength rock will not fail (because the stress concentration is so low). The stress
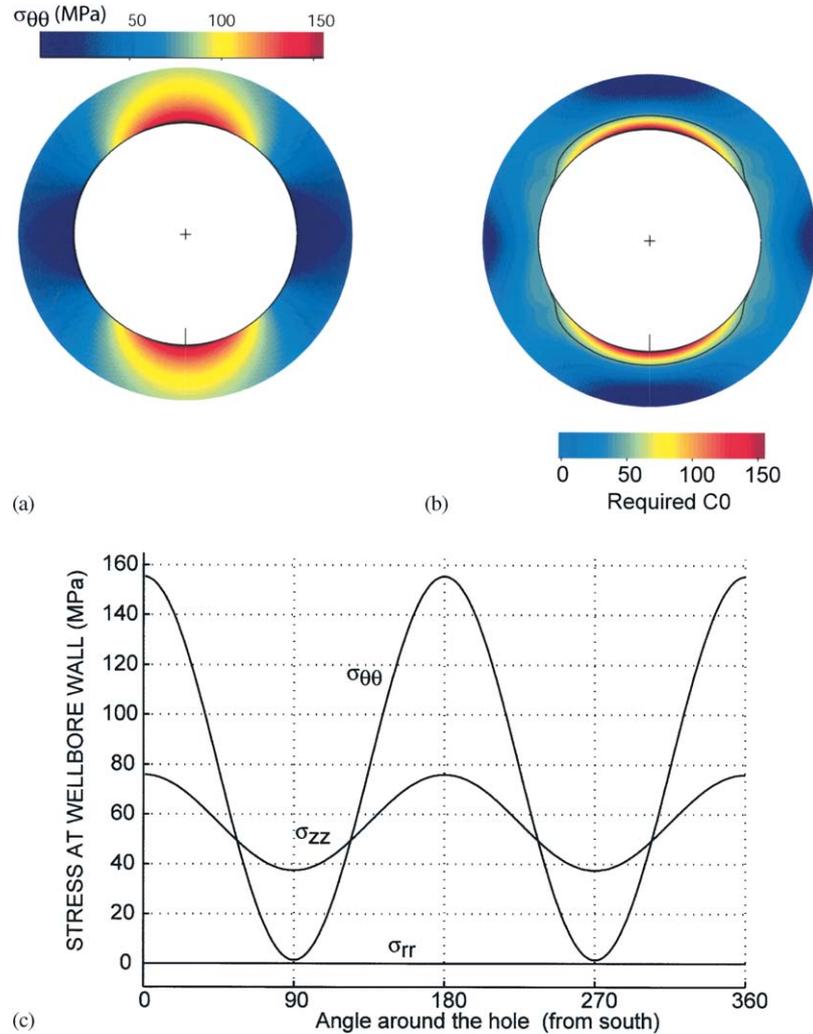
Fig. 7. (a) Circumferential effective stress around a vertical wellbore subjected to east–west compression. The stress magnitudes used for these calculations are listed in the text. (b) The uniaxial compressive rock strength required to avoid failure assuming a Mohr–Coulomb failure criterion and a coefficient of internal friction of 1.0. The contour line indicates the initial zone of failure around the well for a strength of 45 MPa. The principal stresses at each point within this contour exceed the strength of the rock. (c) Variation of the three principal stresses around the wellbore. In the direction parallel to $S_{Hmax}$, $\sigma_{\theta\theta} \approx 0$ because of the large difference of $S_{Hmax}$ and $S_{hmin}$ (note that because $\Delta P = 0$, $\sigma_{rr} = 0$).

concentration exceeds the rock strength everywhere within the contour lines shown on opposite sides of the well, leading to the formation of wellbore breakouts. The breakouts have a finite width ($w_{BO}$, the span of failed rock around the wellbore wall on one side) and initial depth, both of which depend on rock strength for a given stress state. The contour line describes the boundary between the zones where the stress concentration exceeds the strength (as defined above) and where it does not. As discussed further below, once a breakout has formed, the stress concentration increases in the area of breakout formation. Thus, the zone of initial wellbore failure predicted by this contour line does not describe the final shape of the breakout as the resulting stress concentration will cause the breakout to deepen but not widen.

Compressive and tensile failure of the wellbore is easy to consider in terms of the stresses acting right at its wall by substituting $r = R$ in Eqs. (7)–(9). At the wellbore wall, the effective hoop stress and radial stress at the wellbore wall are given by the following equations:

$$\sigma_{\theta\theta} = S_{hmin} + S_{Hmax} - 2(S_{Hmax} - S_{hmin})\cos 2\theta \\ - 2P_p - \Delta P - \sigma^{\Delta T}, \tag{10}$$

$$\sigma_{rr} = \Delta P, \tag{11}$$

where $\Delta P$ is the difference between the wellbore pressure (mud weight, $P_m$) and the pore pressure. The effective stress acting parallel to the axis of a vertical wellbore is

$$\sigma_{zz} = S_v - 2v(S_{Hmax} - S_{hmin})\cos 2\theta - P_p - \sigma^{\Delta T}, \tag{12}$$

where $v$ is Poisson's ratio. At the point of minimum compression around the wellbore (i.e., at $\theta = 0°$, $180°$ parallel to $S_{hmin}$), Eq. (10) reduces to

$$\sigma_{\theta\theta}^{min} = 3S_{hmin} - S_{Hmax} - 2P_p - \Delta P - \sigma^{\Delta T}. \tag{13}$$
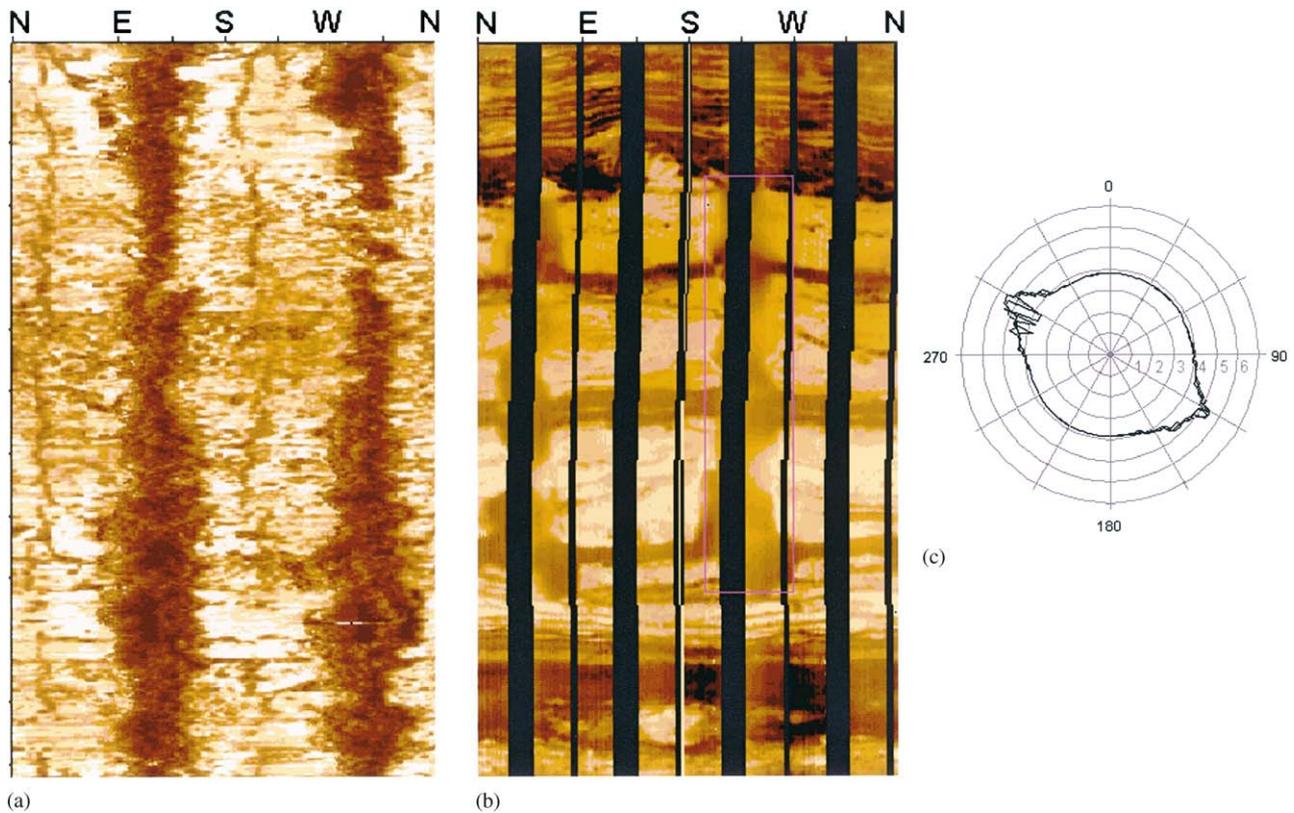
Fig. 8. (a–c) Image logs of a well with wellbore breakouts. These are manifest as dark bands (low reflection amplitudes) on opposite sides of the well in ultrasonic televiewer image logs (UBI Well A) and out-of-focus zones on electrical imaging logs (FMI Well B). By making cross sections of Well A, it is possible to clearly identify wellbore breakouts as shown on the right. Note also the existence of drilling-induced tensile fractures 90° from the breakouts.

At the point of maximum stress concentration around the wellbore (i.e., at $\theta = 90°$, $270°$ parallel to $S_{Hmax}$)

$$\sigma_{\theta\theta}^{max} = 3S_{Hmax} - S_{hmin} - 2P_p - \Delta P - \sigma^{\Delta T}, \qquad (14)$$

such that the difference between the two is

$$\sigma_{\theta\theta}^{max} - \sigma_{\theta\theta}^{min} = 4(S_{Hmax} - S_{hmin}). \qquad (15)$$

Eq. (15) corresponds to the amplitude of the sinusoidal variation of hoop stress around the wellbore shown in Fig. 7c. This four-fold increase in the far-field stress difference in principal stresses explains why observations of wellbore failures can be used to reliably indicate the direction of far-field stresses in vertical wells.

The most reliable way to detect wellbore breakouts is through the use of types of image logs. As shown in Fig. 8a in a standard *unwrapped* wellbore image from an ultrasonic borehole televiewer. Breakouts appear as dark bands of low reflectance on opposite sides of the well [35]. Because interactive digital processing allows cross-sections of a well (such as that shown in Fig. 8c) to be easily displayed [36], it is straightforward to determine both the orientation and opening angle, $w_{BO}$, of the breakouts. The two pairs of radial lines shown define the edges of the breakouts; the width is the difference in these azimuths. Breakouts form symme-

trically on both sides of the well, but the orientations of the breakouts on each side of a well are documented independently. The two *out-of-focus* zones on opposites sides of the well in the FMI image shown in Fig. 8b also correspond to breakouts. These result from poor contact between the wellbore wall and the pad upon which the electrode array is mounted.

It is easily seen in Eq. (10) that if we raise mud weight, $\sigma_{\theta\theta}$ decreases (and $\sigma_{rr}$ increases) by the same amount at all positions around the wellbore. With respect to wellbore failure, two phenomena are important to note. First, with respect to compressive failures, the zone of failure is much smaller [35] which demonstrates why it is possible to stabilize wellbores by increasing the mud weight. The second point of note is that as $\sigma_{\theta\theta}$ decreases, the wellbore wall can locally go into tension at the azimuth of $S_{Hmax}$, leading to the occurrence of drilling-induced tensile fractures. The formation of drilling-induced tensile fractures will not lead to a hydraulic fracture propagating away from the wellbore (which could cause lost circulation) unless the mud weight exceeds the least principal stress.

Because they do not propagate any significant distance away from the wellbore wall and thus have no appreciable affect on drilling, wellbore image logs are
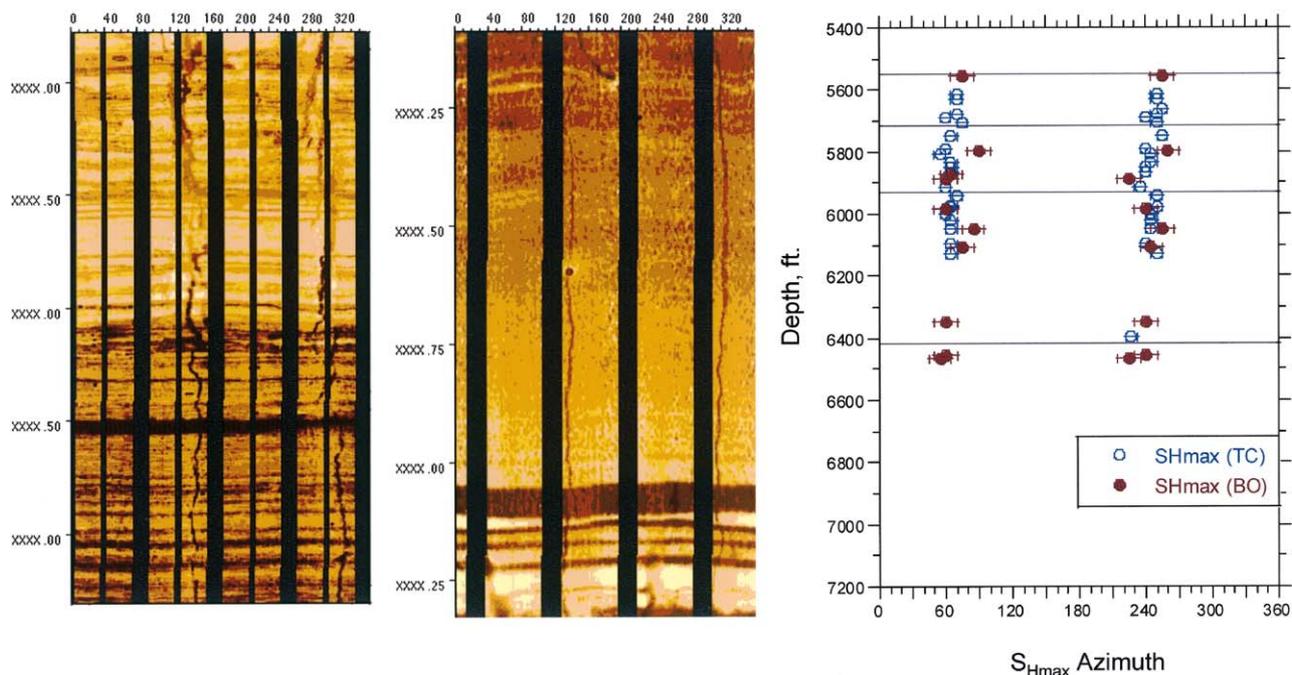
Fig. 9. Drilling-induced tensile fractures in two electrical image logs in the northern North sea. The plot on the right shows that the direction of $S_{Hmax}$ determined from the breakouts and tensile fractures in a well in the San Joaquin valley of California are exactly the same.

essentially the only way to know if drilling-induced tensile fractures are present in a well. This can be seen quite clearly in the two examples of electrical image logs in Fig. 9. As predicted by the simple theory discussed above, the fractures form on opposite sides of the wellbore wall and are parallel to the axis of the wellbore. Note also that in the ultrasonic televiewer image shown in Fig. 8a, there are tensile fractures on opposite sides of the wellbore wall which are oriented $90°$ from the midpoints of the wellbore breakouts. In other words, this well was failing simultaneously in compression and tension as it was being drilled. However, because the tensile fractures did not affect the drilling process, and the breakouts are not excessively large and hence do not cause problems with wellbore stability, the existence of these failures was not known during drilling. In Fig. 9c, the orientation of $S_{Hmax}$ determined from breakouts and drilling-induced tensile fractures in a section of a well in the San Joaquin Valley of California are shown (the orientation of breakouts is shifted $90°$ as they form at the azimuth of $S_{hmin}$). Note that the breakouts and tensile fractures form on opposite sides of the well, $180°$ apart, and the breakouts and tensile fractures form $90°$ apart, exactly as predicted on the basis of the simple theory described above.

Fig. 10 is a stress map of the Timor sea [37], constructed by determination of the orientation of abundant breakouts and tensile fractures that were present at depth in numerous wells. In each well the variation of the maximum horizontal stress direction

determined from the breakouts and tensile fractures is less than $10°$. Note that in each subregion, the stress field is remarkably uniform. Although the average stress orientation in the area seems clearly to correspond to the convergence direction between Australia and Indonesia, the origin of the variations among the subregions in this tectonically active area is not known.

To illustrate how robust drilling-induced tensile fractures are as stress indicators, a stress map of the Visund field in the northern North Sea is shown in Fig. 11 (after Wiprut and Zoback [38]) A very uniform stress field is observed. Drilling-induced tensile fractures were observed in four vertical wells and one deviated well (A–E). The depth intervals logged are shown in white in the lower right corner of the figure and the intervals over which the tensile fractures were observed are shown by the black lines. The rose diagrams show the orientation and standard deviation of the drilling-induced tensile fractures observed in each well as well as a compilation of the 1261 observations made in all of the wells. Note that numerous observations in each well indicate very uniform stress orientations with depth (standard deviations of only $\sim 10°$). As these observations come from depths ranging between 2500 and 5200 m and from wells separated by up to 20 km, it is clear that the stress field is spatially uniform.

Most of the data used to determine the orientation of breakouts come from magnetically oriented four-arm caliper data which are part of the dipmeter logging tool that is commonly used in the petroleum industry.
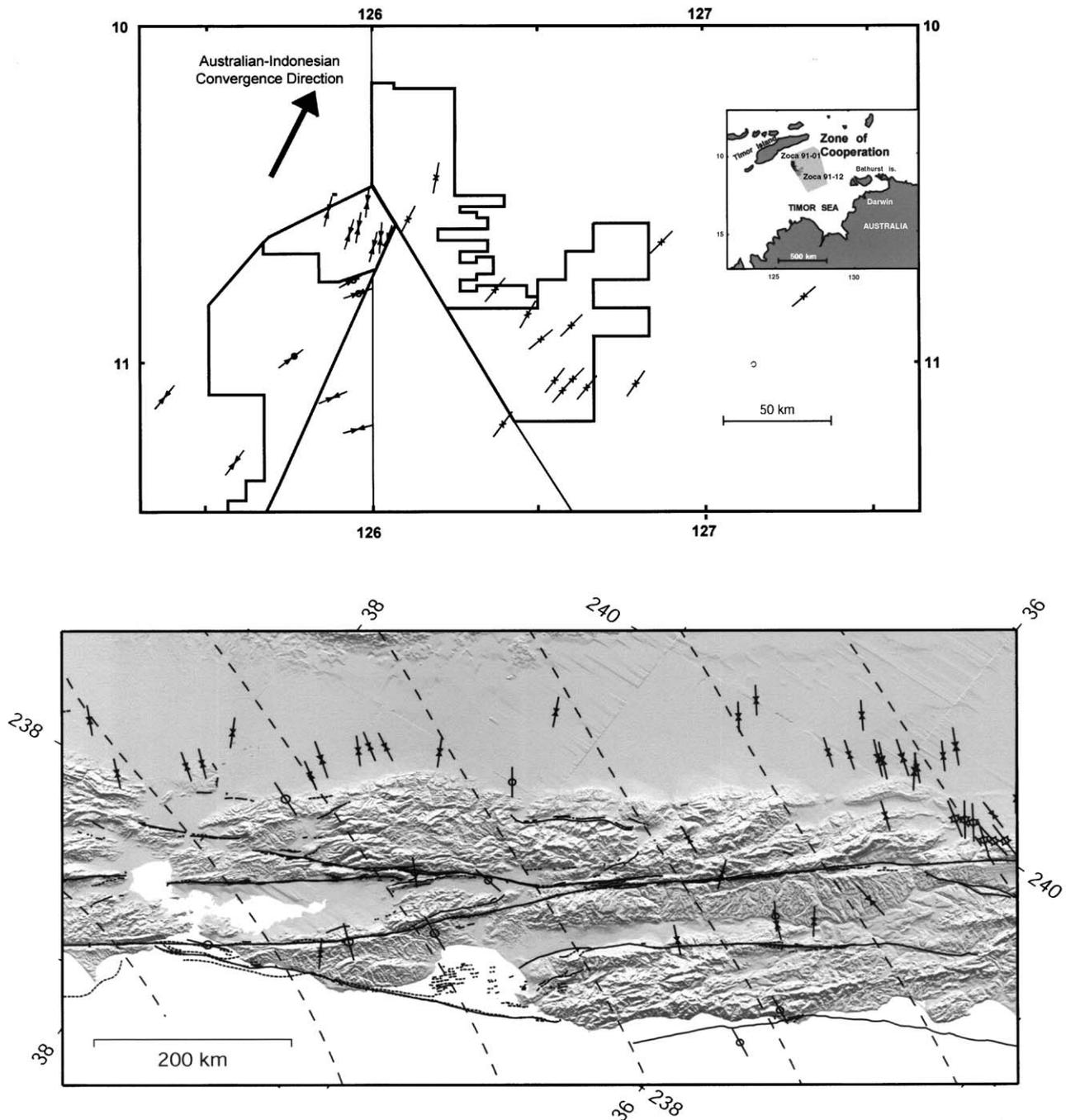
Fig. 10. Stress maps of the Timor sea (above, after Castillo et al. [37]) and central California (below, after Zoback et al. [39]) based on the orientation of wellbore breakouts. Observations of drilling-induced tensile fractures were also used in the Timor Sea study.

Despite the relatively low sensitivity of this technique, with sufficient care it is possible to use four-arm caliper data to reliably determine breakout orientations. This was clearly demonstrated in western California (Fig. 10b, from [39]) where $S_{Hmax}$ orientations obtained from analysis of breakouts with four-arm caliper data (inward pointed arrows) yield consistent stress orientations that correlate well with earthquake focal plane mechanisms (data points with circle in the center) and

young geologic indicators of deformation (the trends of fold axes and active RF) [40–42]. The basis and criteria associated with creating integrated maps of contemporary tectonic stress are those developed by Zoback ML and Zoback MD [6,7,43] and subsequently used in the World Stress Map Project [8].

While the analysis of wellbore breakouts with four-arm caliper data appears to be quite straightforward, it is important not to misinterpret key seats (grooves in the
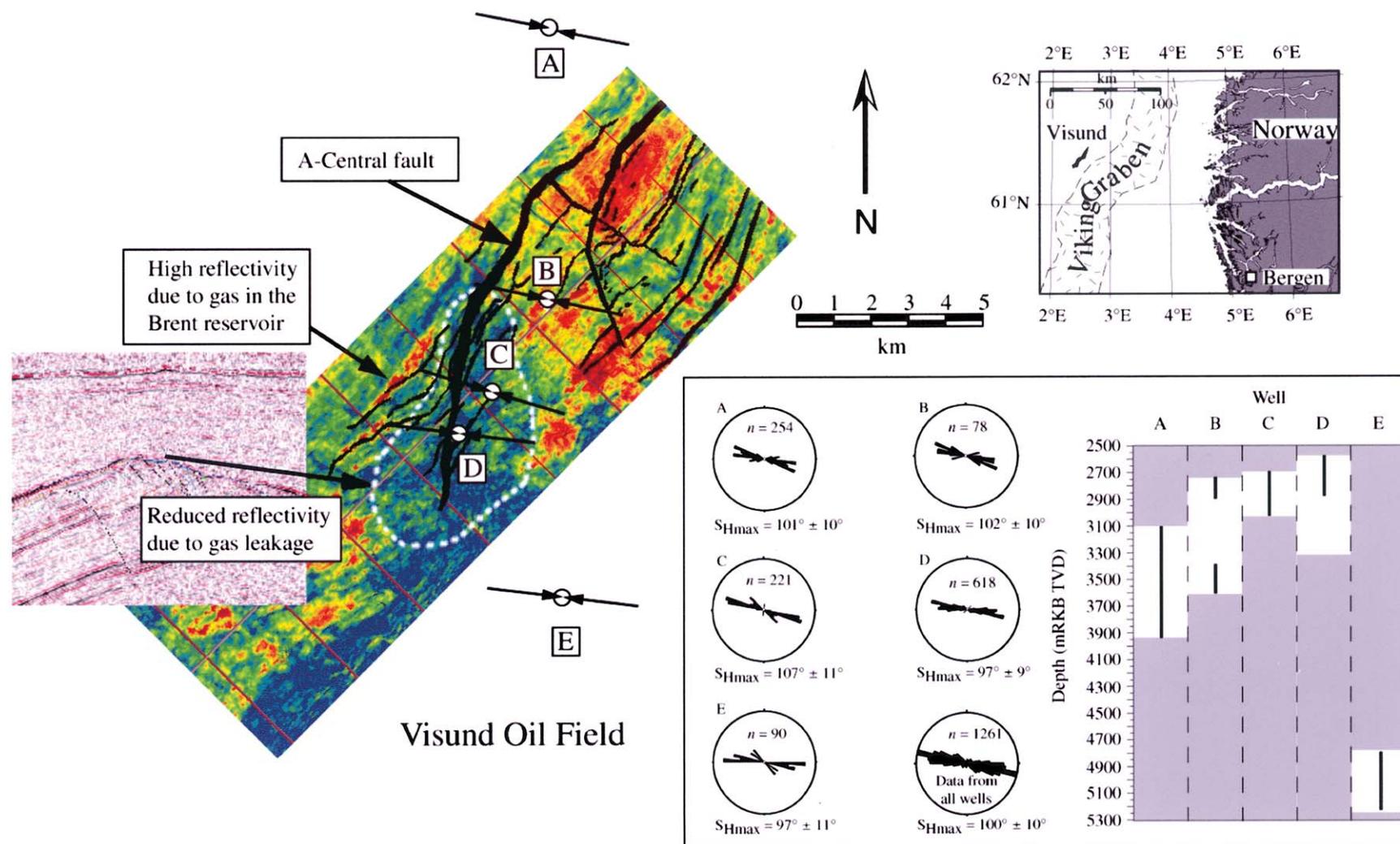
Fig. 11. Stress orientation in five wells in the Visund field determined with drilling-induced tensile fractures by Wiprut and Zoback [38]. The tensile fractures were abundant over hundreds of meters in each well and reveal a remarkably uniform stress orientation within and between the various wells. Note the histograms that show that hundreds of observations in three of the wells have a standard variation less than 10°.

side of the well caused by the rubbing of pipe) or washouts (enlargements of the entire wellbore circumference) as stress-induced breakouts. Plumb and Hickman [44] offered straightforward criteria for the analysis of caliper data to prevent such problems and suggested the following definitions to help properly interpret four-arm caliper logs: *Breakouts* are wellbore enlargements caused by stress-induced failure of a well occuring 180° apart. In vertical wells, breakouts occur at the azimuth of minimum horizontal stress ($S_{hmin}$) and have a consistent orientation within a given well or field. One pair of caliper arms measures the size of the drill bit whereas the orthogonal pair measures a large diameter. The logging tool does not rotate with depth in the breakouts. *Washouts* represent essentially complete failure of the wellbore such that both sets of arms of the four-arm caliper are larger than the diameter of the drill bit. *Keyseats* are an asymmetrical notching of the well caused by mechanical wear of the borehole at its top or bottom. It is also useful to use a wellbore deviation criterion to help distinguish keyseats from breakouts. Even in near-vertical wells, one should never consider enlargements of the wellbore that are essentially parallel (within 10–15°) to the well deviation direction as indicators of wellbore breakouts. Over the past 17 years, numerous studies have shown that if carefully analyzed, caliper-determined breakout orientations are remarkably consistent in a given well and a given oil-field ([41,45–47]), and yield a reliable measure of stress orientation in many parts of the world. Such data are an integral part of the World Stress Map database (http://www-wsm.physik.uni-karlsruhe.de).

## 6. Drilling-induced tensile fractures and the magnitude of $S_{Hmax}$

As mentioned above, drilling-induced tensile fractures occur in vertical wells whenever there is a significant difference between the two horizontal stresses. In fact, it is straightforward to show that the conditions for the occurrence of drilling-induced tensile fractures around a wellbore and the values of $S_{hmin}$ and $S_{Hmax}$ associated with an SS faulting regime in frictional equilibrium are essentially identical. To see this we simply re-write Eq. (3) for the case frictional equilibrium and $\mu = 0.6$

$$S_{Hmax} = 3.1 S_{hmin} - 2.1 P_p$$

and, re-write it again (for reasons that will soon be evident) as

$$S_{Hmax} = 3 S_{hmin} - 2 P_p + 0.1(S_{hmin} - P_p). \qquad (16)$$

If we now revisit Eq. (13) that describes the formation of tensile fracture in the wall of a vertical wellbore and, for the moment, assume that the cooling stress, $\sigma^{\Delta T}$,

excess mud weight, $\Delta P$, and tensile strength are negligible, a tensile fracture will form at the wellbore wall when

$$\sigma_{\theta\theta}^{min} = 3 S_{hmin} - S_{Hmax} - 2 P_p = 0 \qquad (17)$$

or

$$S_{Hmax} = 3 S_{hmin} - 2 P_p. \qquad (18)$$

Because the last term in Eq. (16) ($0.1(S_{hmin} - P_p)$) is usually quite small, Eqs. (16) and (18) are nearly identical. In other words, for combinations of $S_{hmin}$ and $S_{Hmax}$ which result in frictional equilibrium in the crust (for $\mu \sim 0.6$), a vertical wellbore wall will go into tension at the azimuth of $S_{Hmax}$ and drilling-induced tensile fractures would be expected without appreciable excess mud weight or wellbore cooling.

This can be illustrated graphically using the type of plot shown in Fig. 2 that defines possible stress magnitudes at any given depth based on the frictional strength of the crust. In Fig. 12a, we illustrate the fact that for $\Delta T = \Delta P = 0$, the line on the periphery of the polygon indicating the magnitude of $S_{Hmax}$ as a function of $S_{hmin}$ for SS fault equilibrium is almost exactly the same as the line representing Eq. (13) (or Eq. (18)) for zero tensile strength which is shown in blue.

It was noted above (and obvious in Eq. (13)) that tensile fracture formation will occur more easily (i.e., at lower values of $S_{Hmax}$ for a given value of $S_{hmin}$) if the ECD is significantly above the pore pressure or if the drilling mud is significantly cooler than the rock. The effect of temperature on stresses around the wellbore is obviously time-dependent, in the sense that the longer the rock is in contact with the wellbore fluid the further away from the hole the temperature perturbation will propagate. To simplify this problem, one can assume that the material is impermeable, and relatively simple integral equations can be written for the magnitudes of $\sigma_{\theta\theta}$ and $\sigma_{rr}$ as a function of radial position $r$ and time $t$ [48]. Although the exact solution for the temperature distribution near a constant-temperature wellbore is a series expansion [49], solutions which approximate the temperature using the first two terms of the expansion give sufficiently accurate results close to the hole, and the stresses become:

$$\sigma_{\theta\theta} = [\alpha_t E \Delta T/(1-v)] [1/(2\rho) - \tfrac{1}{2} - \ln \rho) I_0^{-1} - (\tfrac{1}{2} + 1/(2\rho)], \qquad (19)$$

$$\sigma_{rr} = [\alpha_t E \Delta T/(1-v)] [1/(2\rho) + \tfrac{1}{2} - \ln \rho) I_0^{-1} - (\tfrac{1}{2} - 1/(2\rho)], \qquad (20)$$

where $\alpha_t$ is the linear coefficient of thermal expansion and $E$ is Young's modulus (see also [18])

$$I_0^{-1} = \frac{1}{2\pi i} \int_{-\infty}^{0_+} \frac{e^{[4\tau_z/\sigma^2]^z}}{z \ln z} \, dz.$$
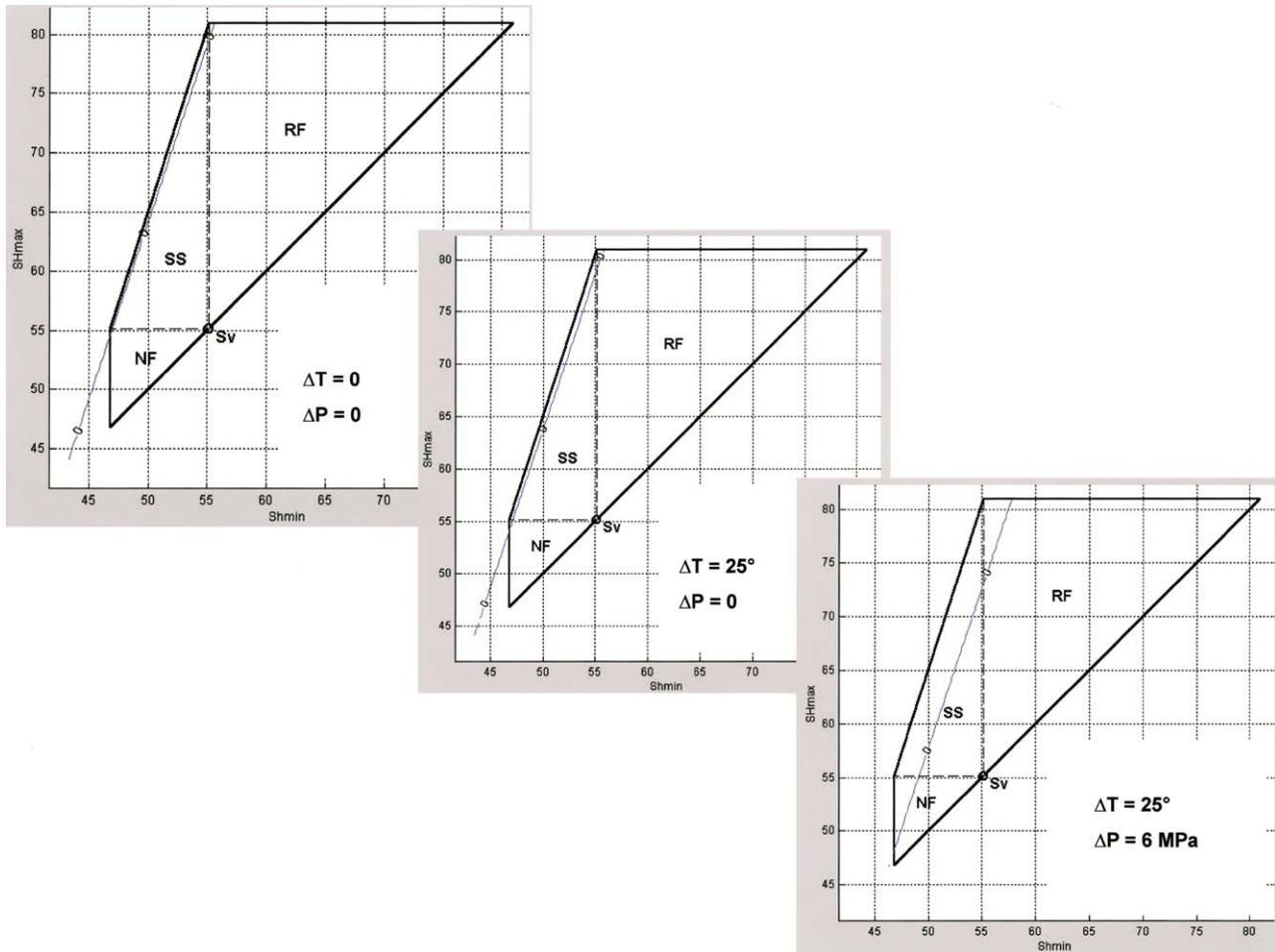
Fig. 12. Polygons showing possible stress magnitudes at depth (similar to Fig. 2) that also shows (blue lines) the magnitude of $S_{Hmax}$ required to induce drilling-induced tensile fractures (after Moos and Zoback [18]). The figure in the upper left demonstrates that in the absence of excess wellbore pressure and wellbore cooling, the relationship between $S_{hmin}$ and $S_{Hmax}$ required to cause tensile fractures is the same as that associated with active SS faults. With cooling (center) and cooling and excess pressure (right) tensile fractures are induced at lower values of $S_{Hmax}$ for a given value of $S_{hmin}$.

Once steady state has been reached, the change in the hoop stress is given by

$$\sigma_{\theta\theta}^{\Delta T} = (\alpha_t E\,\Delta T)/(1-v). \qquad (21)$$

where $\alpha_t$ is a strong function of silica content because the coefficient of thermal expansion of quartz is an order of magnitude higher than other rock forming minerals. For drilling-induced tensile fractures in well D in the Visund field of the northern North Sea (Fig. 11), wellbore cooling of $\sim 30^\circ$C at a depth of $\sim 2750$ m resulted in $\sigma_{\theta\theta}^{\Delta T} = 1.7$ MPa based on: $\alpha = 2.4 \times 10^{-6\,\circ}$C$^{-1}$ (corresponding to a rock composed of 30% quartz), $E = 1.9 \times 10^4$ MPa (from the measured $P$-wave velocity) and $v = 0.2$ (based on the $P$ to $S$-wave velocity ratio).

Fig. 12b shows the effect of wellbore cooling of $25^\circ$C on the formation of drilling-induced tensile fractures utilizing Eq. (13). As can be seen through comparison with Fig. 12a, the result of moderate cooling makes it slightly easier for drilling-induced tensile fractures to be induced. That is, for a given value of the $S_{hmin}$, tensile fractures can occur at a slightly lower value of $S_{Hmax}$. Of course, significant cooling occurs in geothermal wells and this effect is much greater. As mud weights during drilling (i.e., that which corresponds to the ECD) above the pore pressure also encourage the formation of drilling-induced tensile fractures. Fig. 12c shows how $25^\circ$C of wellbore cooling and 6 MPa of excess mud weight affect the formation of tensile fractures. Note that modest increases in mud weight are much more influential on the formation of tensile fractures than are modest amounts of wellbore cooling. This will be important when we use observations of drilling-induced tensile fractures for estimating the magnitude of $S_{Hmax}$.

It is clear from Fig. 12 how the observation of drilling-induced tensile fractures in vertical wells allow us to estimate $S_{Hmax}$ if pore pressure, $S_v$ and $S_{hmin}$ are known. For any given value of $S_{hmin}$, the periphery of

the polygon provides a reasonable upper bound for $S_{Hmax}$ because it cannot be significantly larger than the frictional strength of the crust. However, if tensile fractures are present, it is also clear that $S_{Hmax}$ must be at least as large as the value shown by the blue line or tensile fractures would not form. Hence, the observation of the drilling-induced tensile fractures provides a lower bound for the magnitude of the least principal stress. In fact, as pointed out by Brudy et al. [16], this value of $S_{Hmax}$ must also be considered as a lower-bound estimate because the drilling-induced tensile fractures might have occurred even if there had been no excess mud weight or cooling of the wellbore wall. For the case of Visund, Wiprut et al. [26] went to great pains (through analysis of all of the daily drilling reports) to correctly estimate both the ECD and amount of cooling in the wells shown in Fig. 11 as a function of depth. Being careful not to evaluate any tensile fracture where

the ECD may have been affected by a bit-trip or swab-and-surge activities, the values of $S_{Hmax}$ shown in Fig. 5 were obtained. While there is a significant range of uncertainty in these values, it is clear that $S_{Hmax}$ is appreciably greater than the overburden.

## 7. Wellbore breakouts and the determination of $S_{Hmax}$

As discussed below, breakouts form in the area around a wellbore where the stress concentration exceeds the rock strength. As first pointed out by Zoback et al. [35], once a breakout forms, the stress concentration around the wellbore is such that breakouts will tend to deepen. This was illustrated theoretically as shown in Fig. 13a. Subsequent work on the manner in which breakout growth would eventually stabilize confirmed this result [50], as did laboratory
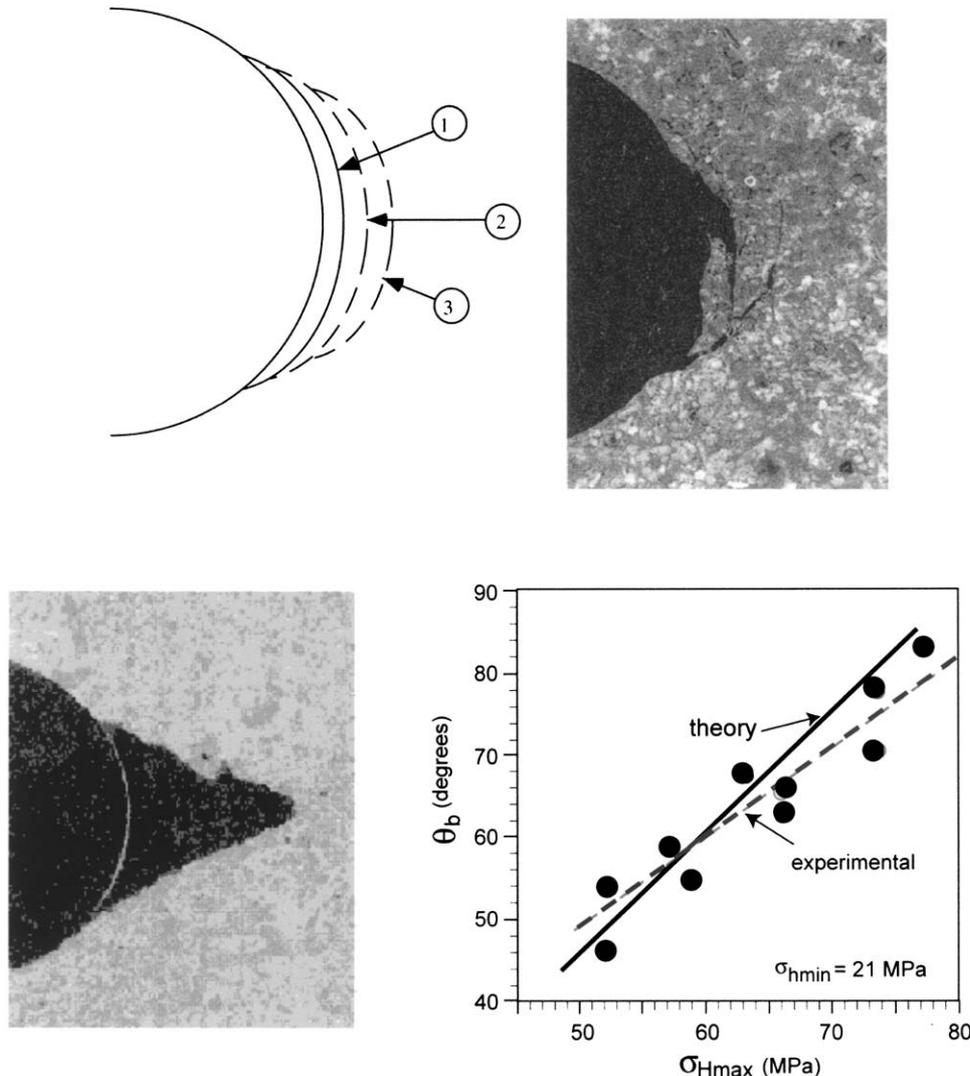


Fig. 13. The theoretical growth of a breakout after initial formation (upper left, after Zoback et al. [35]). Note that the breakouts deepen but do not widen. The photographs of breakouts formed in laboratory experiments confirm this as well as the relationship between stress magnitude and breakout width (lower right, after Haimson and Herrick [51]).

studies of breakout formation by Haimson and Herrick [51]. Photographs of breakouts formed in these laboratory experiments are shown in Figs. 13b and c and the excellent comparison between measured breakout widths and theoretically predicted ones are shown in Fig. 13d.

Because breakout width is expected to remain stable as breakout growth occurs, Barton et al. [52] proposed a methodology for determination of $S_{Hmax}$ when the rock strength is known utilizing observations of breakout width. Because the stress concentration at the edge of a breakout is in equilibrium with the rock strength, they derived the following:

$$S_{Hmax} = \frac{(C + 2P_p + \Delta P + \sigma^{\Delta T}) - S_{hmin}(1 + 2\cos 2\theta_b)}{1 - 2\cos 2\theta_b}. \quad (22)$$

This methodology has been successfully used in a number of deep scientific drill holes around the world including Fenton Hill, New Mexico [52], Cajon Pass, California [53] and the KTB, Germany [10]. In each case the range of values based on Eq. (22) are consistent with estimates independently derived from drilling-induced tensile fractures as well as expected values on the basis of earthquake focal mechanisms. For example, in areas characterized by both SS and N faulting earthquakes, $S_{Hmax} \approx S_v$. At both the Fenton Hill and Cajon Pass sites, the values derived with Eq. (22) yielded such estimates.

Another way to envision utilization of Eq. (22) for determination of $S_{Hmax}$ is in the context of the diagrams shown in Fig. 12. The example shown in Fig. 14 is for a deep oil well in Australia that was drilled into very strong rock (unconfined compressive strength $20,000 \pm 2000$ psi). Both wellbore breakouts (average width $45°$) and drilling-induced fractures are present in the well. The steep line shown in blue is similar to those shown in Fig. 12, the value of $S_{Hmax}$ required to cause drilling-induced tensile fractures. The red lines correspond to the value of $S_{Hmax}$ required to cause breakouts with a width of $45°$ for rocks of the different strengths indicated. As the magnitude of $S_{hmin}$ is approximately the vertical stress, $S_{Hmax}$ is approximately 130 MPa. It is straightforward to show that if $S_{Hmax}$ was appreciably smaller, the breakout widths would have been smaller (or possibly not have formed). Similarly, if $S_{Hmax}$ was appreciably larger, the breakout width would have been greater. Thus, the observations of breakout width and occurrence of tensile fractures yield the same range of values of $S_{Hmax}$, which indicate an SS stress state in frictional equilibrium. To utilize these techniques, however, independent knowledge of pore pressure, the vertical stress, the least principal stress and rock strength are needed for estimation of $S_{Hmax}$ from breakout width.
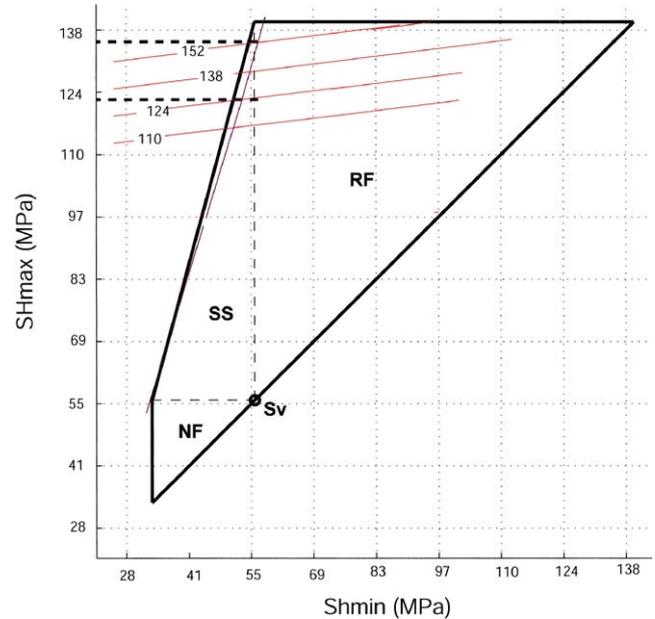


Fig. 14. Polygon showing possible stress states at depth for the case study described in the text. The heavy dashed lines show the magnitude of $S_{Hmax}$ (for a given value of $S_{hmin}$) that is required to cause breakouts with a width of $45°$ for the rock strengths shown. As in Fig. 12, the blue line indicates the stress values associated with the initiation of tensile fractures in the wellbore wall.

There are two extensions of this discussion that are worth noting. First, if there were no information on rock strength available, we could not have used the observations of breakout width to constrain $S_{Hmax}$. However, because there were tensile fractures present, we could deduce the strength as the magnitude of $S_{Hmax}$ would have been determinable from the occurrence of tensile fractures alone. Had the strength been less than about 20,000 psi, the breakout width would have been much greater. Had the strength been greater, the breakouts would have been narrower (or absent altogether).

## 8. Wellbore failures in deviated wells

Because a large fraction of the wells being drilled for oil and gas production are highly deviated, horizontal or drilled with complex trajectories, it is necessary to have techniques for stress determination in such wells. In a deviated well, the principal stresses acting in the vicinity of the wellbore wall are not aligned with the wellbore axis (Fig. 15a). Despite the complexities associated with such cases, we will fundamentally consider whether the principal stresses acting in a plane tangential to the wellbore wall, $\sigma_{tmax}$ and $\sigma_{tmin}$ (and $\sigma_{rr}$ acting normal to the wellbore wall) are such that wellbore will go into failure. We will define the angle between the axis of the wellbore and the plane normal to $\sigma_{tmin}$ as $\omega$ (Fig. 15a), and consider stress variations as a function

(a)

(b)

| Rotation Angle | Geographic | Stress |
|:---:|:---:|:---:|
| $\alpha$ | X (N) | $x_s$ |
| $\beta$ | Y (E) | $y_s$ |
| $\gamma$ | Z (Down) | $z_s$ |

(c)

(d)
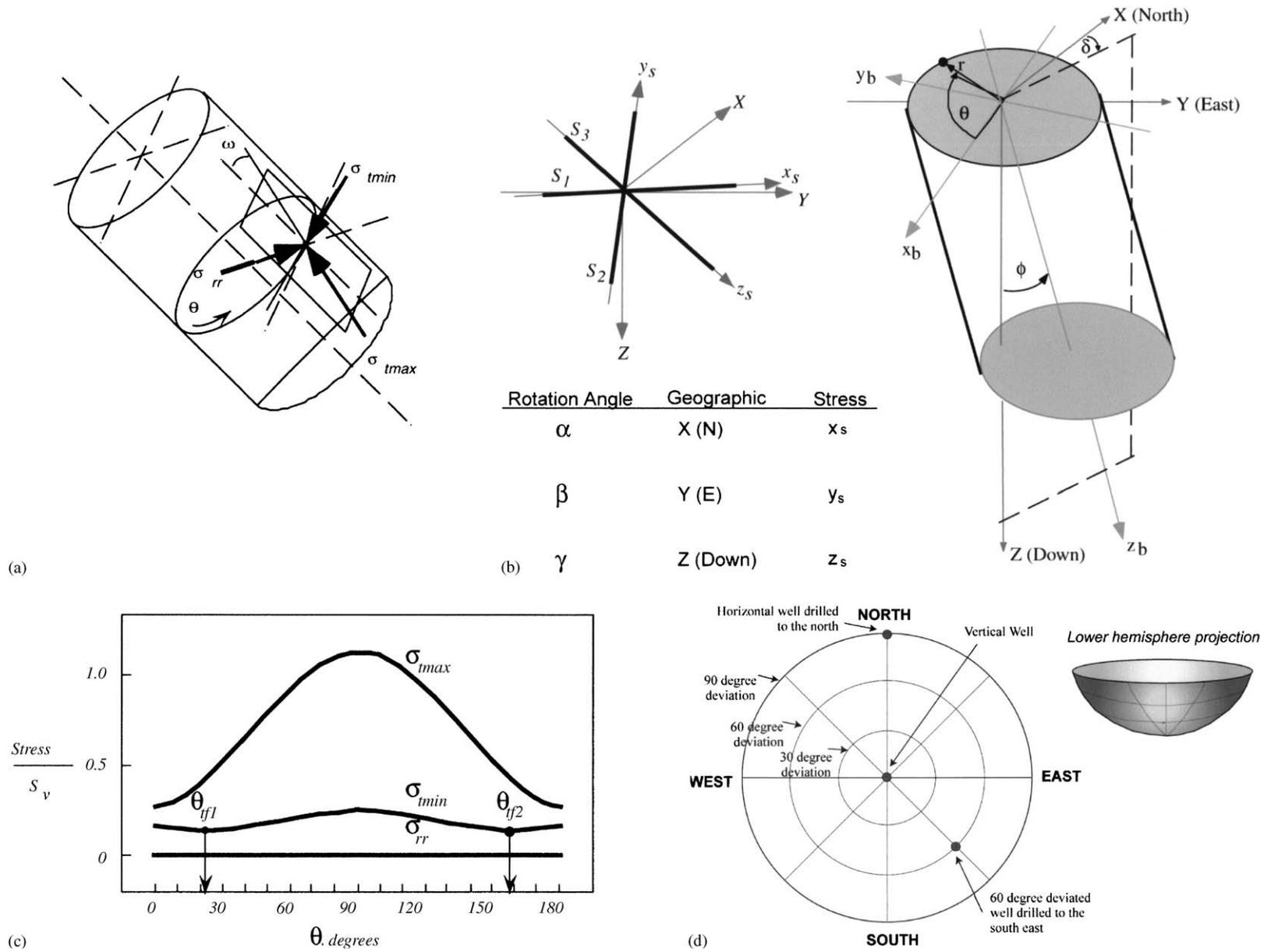
Fig. 15. (a) Stresses acting in the wall of an arbitrarily oriented well, (b) coordinate system used to transform knowledge of principal stresses, to that around the wellbore, (c) variation of principal stresses around an arbitrarily oriented wellbore, and (d) lower-hemisphere projection used to display relative stability of wells with different deviations and azimuth.

of position around the well going clockwise from the bottom (Fig. 15b). As will be shown below, in the case of an arbitrarily deviated well there is no simple relation between the orientation of far-field stresses and the position around the well at which either compressive or tensile failure might possibly occur.

To consider failure in a well of any orientation, we must define three coordinate systems (Fig. 15c); (1) a geographic coordinate system, $X$, $Y$ and $Z$ oriented north, east and vertical (down), (2) a stress coordinate system, $x_s$, $y_s$ and $z_s$ (corresponding to the orientations $S_1$, $S_2$, and $S_3$) and (3) the wellbore coordinate system $x_b$, $y_b$ and $z_b$ where $x_b$ is radial, pointing to the bottom of the well $z_b$ is down along the wellbore axis and $y_b$ is orthogonal in a right-hand coordinate system. We will evaluate wellbore failure as a function of angle from the bottom of the well in a clockwise direction given by the angle $\theta$.

Following [54], we will utilize tensor transformations to evaluate stress in the three coordinate systems of interest. In tensor notation, the principal stresses are given by

$$S_s = \begin{pmatrix} S_1 & 0 & 0 \\ 0 & S_2 & 0 \\ 0 & 0 & S_3 \end{pmatrix}. \tag{23}$$

To rotate these stresses into a wellbore coordinate system, we will need to know how to transform the stress field first into a geographic coordinate system using the angles $\alpha$, $\beta$, $\gamma$ (Fig. 15c). This is done using

$$\begin{pmatrix} x_s \\ y_s \\ z_s \end{pmatrix} = R_s \begin{pmatrix} X \\ Y \\ Z \end{pmatrix}, \tag{24}$$

where

$$R_s = \begin{pmatrix} \cos\alpha\cos\beta & \sin\alpha\cos\beta & -\sin\beta \\ \cos\alpha\sin\beta\sin\gamma - \sin\alpha\cos\gamma & \sin\alpha\sin\beta\sin\gamma + \cos\alpha\cos\gamma & \cos\beta\sin\gamma \\ \cos\alpha\sin\beta\cos\gamma + \sin\alpha\sin\gamma & \sin\alpha\sin\beta\cos\gamma - \cos\alpha\sin\gamma & \cos\beta\cos\gamma \end{pmatrix}. \tag{25}$$

To transform the stress field from the geographic coordinate system to the borehole system, we will use

$$\begin{pmatrix} x_b \\ y_b \\ z_b \end{pmatrix} = R_b \begin{pmatrix} X \\ Y \\ Z \end{pmatrix}, \tag{26}$$

where

$$R_b = \begin{pmatrix} -\cos\delta\cos\phi & -\sin\delta\cos\phi & \sin\phi \\ \sin\delta & -\cos\delta & 0 \\ \cos\delta\sin\phi & \sin\delta\sin\phi & \cos\phi \end{pmatrix}. \tag{27}$$

With $R_s$ and $R_b$ defined, we can define the stress in first a geographic and then a wellbore coordinate system using the following transformations:

$$S_g = R_s^T S_s R_s,$$
$$S_b = R_b R_s^T S_s R_s R_b^T, \tag{28}$$

where we define effective stress using the generalized form of the effective stress law described above. We go on to define individual stress components around the well (simplified here for the wellbore wall) as

$$\sigma_{zz} = \sigma_{33} - 2v(\sigma_{11} - \sigma_{22})\cos 2\theta + 4v\sigma_{12}\sin 2\theta,$$
$$\sigma_{\theta\theta} = \sigma_{11} + \sigma_{22} - 2(\sigma_{11} - \sigma_{22})\cos 2\theta$$
$$\qquad + 4\sigma_{12}\sin 2\theta - \Delta P,$$
$$\tau_{\theta z} = 2(\sigma_{23}\cos\theta - \sigma_{13}\sin\theta),$$
$$\sigma_{rr} = \Delta P. \tag{29}$$

So that the principal stresses are given by

$$\sigma_{t\max} = \tfrac{1}{2}(\sigma_{zz} + \sigma_{\theta\theta} + \sqrt{(\sigma_{zz} - \sigma_{\theta\theta})^2 + 4\tau_{\theta z}^2}),$$
$$\sigma_{t\min} = \tfrac{1}{2}(\sigma_{zz} + \sigma_{\theta\theta} - \sqrt{(\sigma_{zz} - \sigma_{\theta\theta})^2 + 4\tau_{\theta z}^2}). \tag{30}$$

To evaluate the stability of wells of any orientation, we will use a lower-hemisphere diagram as illustrated in Fig. 15d, where any point represents a well of a given azimuth and deviation. Vertical wells correspond to a point in the center, horizontal wells correspond to a point on the periphery at the appropriate azimuth and deviated wells are plotted at the appropriate azimuth and radial distance. Fig. 16a shows the relative stability of wells of various orientations. Fig. 16 was calculated using the stress state used in the construction of Fig. 7. The principal stresses are in vertical and horizontal planes and the direction of maximum horizontal stress is east–west. However, Fig. 16 could have been calculated for any arbitrary stress field [55].

The colors in Fig. 16a indicate the width of breakouts for wellbores of any arbitrary orientation at the depth of interest in the prescribed stress state. As can be seen by comparison with Fig. 7, vertical wells are expected to have breakout widths of about 90°. Wellbore deviations up to about 30° have a similar degree of instability, as do wells of any deviation drilled approximately east–west. Highly deviated wells drilled in the north–south direction are quite unstable as breakouts with much greater width would be expected to occur. In fact, near-horizontal wells in this direction would undoubtedly be *washed out* as the breakouts subtend nearly the entire
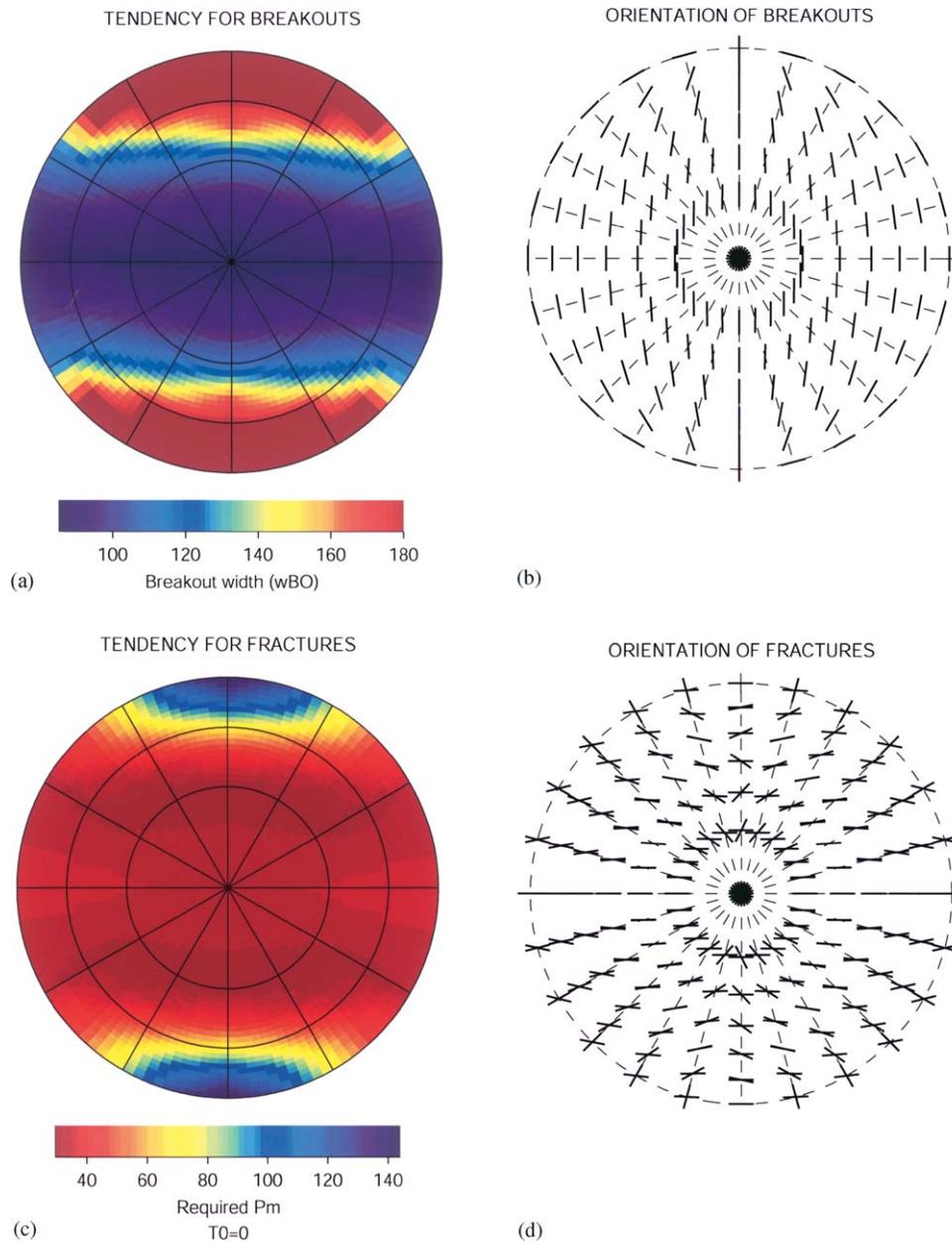
Fig. 16. Lower-hemisphere representations; the relative stability of wellbores of varied orientation with respect to the formation of wellbore breakouts (a,b) and drilling-induced tensile fractures (c,d) (after Peska and Zoback [54]). (a) The width of breakouts in red areas indicate unstable wellbores as nearly the entire circumference of the well fails, (b) orientation of wellbore breakouts (if they form) in a *looking-down-the-well* coordinate system, (c) the tendency of drilling-induced tensile fractures to form in terms of the magnitude of excess mud weight needed to initiate failure, and (d) the orientation of induced tensile failures (see text).

circumference of the well. The orientation of the wellbore breakouts are shown in Fig. 16b in a "looking down the well" reference frame. Thus, a highly deviated well to the north or south would have breakouts on the top and bottom of the well whereas highly deviated wells drilled to the east or west would have breakouts on the side.

Fig. 16c is a similar plot to Fig. 16a except that it represents the tendency for tensile fractures to occur expressed as the magnitude of the wellbore pressure required to induce tensile wall failure of the wellbore wall. The orientation of the tensile fractures is shown in Fig. 16d, where the two lines indicate the position of the tensile fractures around the well and the angle with respect to the wellbore axis (see [54]). As noted by Brudy and Zoback [56] and Peska and Zoback [54], drilling-induced tensile fractures in deviated wells generally occur as echelon pairs of fractures which are inclined to the wellbore wall at the angle $\omega$, referred to above (see Fig. 15a). An example of such fractures in the KTB
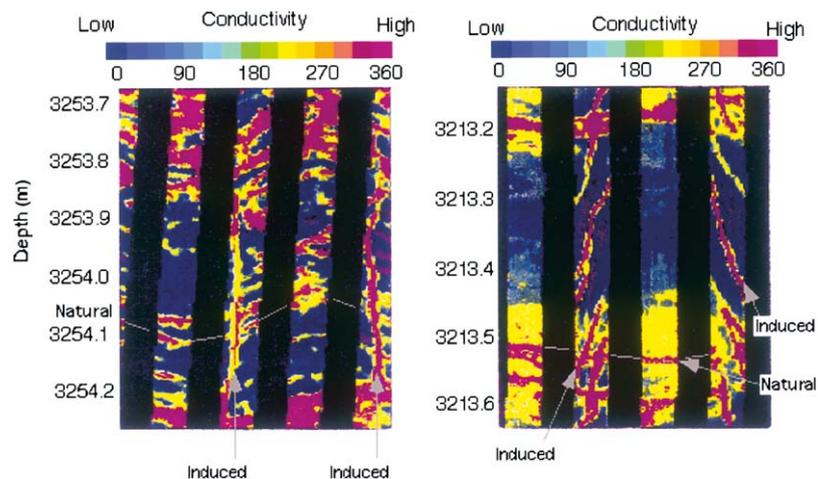
Fig. 17. Electrical resistivity image of drilling-induced tensile fractures observed in the KTB pilot hole (after Peska and Zoback [54]). Nearly all the tensile fractures were axial as shown [16] on the left except in intervals where the stress field is locally perturbed and one principal stress is not vertical resulting in the en echelon tensile fractures shown on the right.

pilot hole is shown in Fig. 17b (after Zoback et al. [57]). Along most of the well paths, the tensile fractures are axial (Fig. 17a) in this near-vertical borehole indicating a near-vertical principal stress. However, in a few sections of the wellbore, the state of stress is locally perturbed by slip on faults (see below) and is rotated away from a horizontal and vertical orientation [16]. In these sections, en echelon drilling-induced tensile fractures such as those shown are observed. Ito et al. [30] discuss how the en echelon tensile fractures at the wellbore wall propagate away from a well and begin to link-up as they turn to become perpendicular to the least principal stress. A similar situation is discussed by Baumgärtner et al. [58] for the case of hydraulically fracturing a vertical well when the least principal stress is vertical (RF regime). Although axial tensile fractures form at the wellbore wall when the $\sigma_{\theta\theta}$ goes to zero as a result of borehole pressurization, the fractures *roll-over* into a horizontal plane as they propagate away from the well.

As the stress state used in the calculations in Fig. 16c are the same as those used in Fig. 7, it is clear that in near-vertical wells, the wellbore pressure at which tensile failure is expected is essentially the same as the pore pressure. In other words, drilling-induced tensile fractures are expected with no excess wellbore pressure. As shown in Fig. 16c, for this stress state, this is true for many wellbore orientations.

## 9. Estimating $S_{Hmax}$ from breakouts and tensile fractures in deviated wells

There are a number of ways in which observations of tensile fractures and breakouts in deviated wells can be used to determine the magnitude and orientation of

$S_{Hmax}$ at depth. The vertical principal stress, $S_v$, and minimum horizontal stress, $S_{hmin}$, are determined in the manner described previously. Thus, in the cases considered below, the wells are significantly deviated but the occurrence of axial drilling-induced tensile fractures in vertical sections of the wells indicates that the principal stresses are vertical and horizontal. In the generalized case of a deviated well in a deviated stress field, LOTs will provide information on the least principal stress, but it would be necessary to do iterative forward modeling of observed wellbore failures to determine principal stress orientations and magnitudes.

In the first case we consider (after Wiprut et al. [26]), drilling-induced tensile fractures were observed in the vertical section of a well in the Visund field of the northern North Sea. Below 2600 m depth, the well gradually increased in deviation with depth at an azimuth of 280° with a *build-and-hold* trajectory (Fig. 18a). Numerous drilling-induced tensile fractures were observed in the near-vertical section of this well as well as other near-vertical wells in the field. The fractures were used in the manner described above to estimate the magnitude and orientation of the maximum horizontal stress (Figs. 5 and 11) after taking care to estimate the ECD and thermal perturbation of the wellbore stress concentration as accurately as possible [26]. One of the interesting observations in this well is that the tensile fractures abruptly ceased at a deviation of 35° (Fig. 18b). In fact, this is exactly what is expected for the stress field shown in Fig. 5. As shown in Fig. 18c, near-vertical wells are expected to fail in tension at mud weights just a few MPa above the pore pressure, in contrast to wells deviated more than 35° that require excess wellbore pressures over 9 MPa to initiate tensile failure. As the ECD was approximately 6 MPa above the pore pressure in the Visund well, there was sufficient
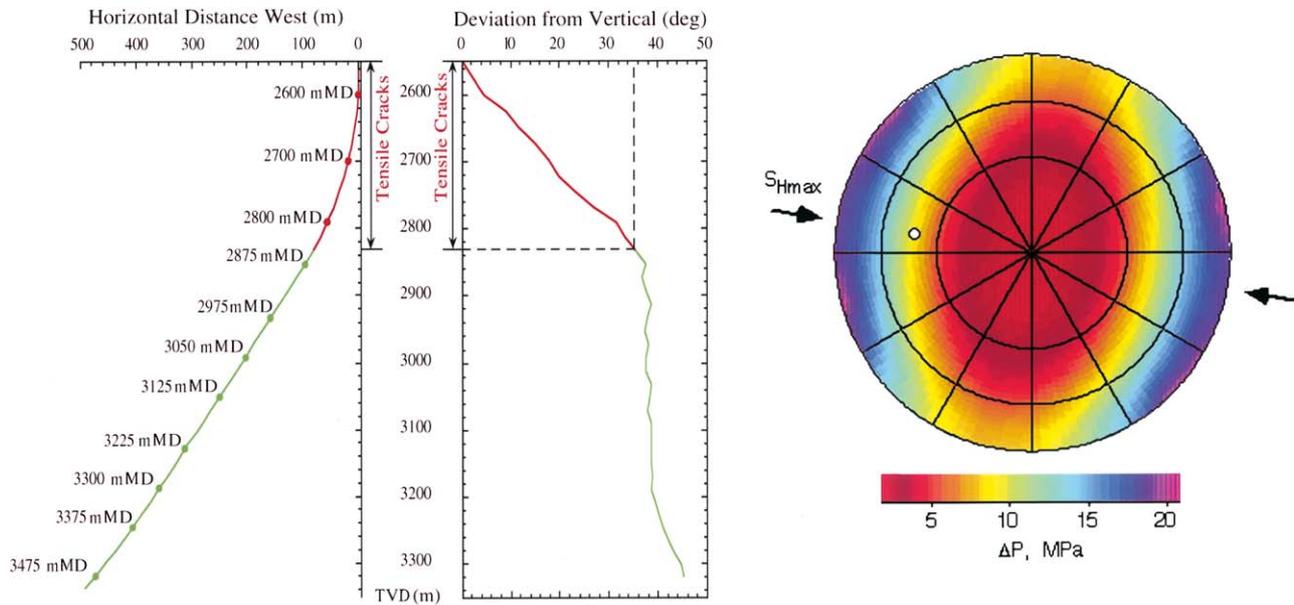
Fig. 18. Drilling-induced tensile fractures were observed in the near-vertical portion of a well in the Visund field in the northern North Sea which abruptly ceased when the well deviated more than 35° (center). As shown in the figure on the right, this result is predicted by the stress state shown in Fig. 5 (after Wiprut et al. [26]).

mud weight to induce tensile fractures in the near-vertical section of the well, but insufficient mud weight to do so in the more highly deviated sections.

This type of forward modeling is quite useful in putting constraints on the magnitude and orientation of $S_{Hmax}$ when observations of wellbore failure are available in deviated wells. As we often have knowledge of the vertical stress and least principal stress, we can use iterative forward modeling to constrain values of $S_{Hmax}$ magnitude and orientation that match the inclination of en echelon tensile failures with respect to the wellbore axis, $\omega$, and their position around the wellbore circumference. As was the case with vertical wells, the absence of drilling-induced tensile fractures in a deviated well allows us to put upper bounds on the magnitude of $S_{Hmax}$.

Because the position of both tensile fractures and breakouts around a deviated wellbore depends on the magnitude and orientation of all three principal stresses (as well as the orientation of the wellbore), independent knowledge of $S_v$ and $S_{hmin}$ enables us to constrain possible values of the orientation and magnitude of $S_{Hmax}$. This technique was used by Zoback and Peska [59] to model the position of breakouts around a deviated well in the Gulf of Mexico to determine the magnitude and orientation of the maximum horizontal stress. As shown in Fig. 19a, the breakouts which occurred in this wellbore will only occur at the position around the wellbore where they were observed if the orientation of $S_{Hmax}$ is at an azimuth of about $136° \pm 8°$. This corresponds to a direction of $S_{hmin}$ that is

orthogonal to the strike of a nearby normal fault (Fig. 19b), exactly as expected from faulting theory. The estimate of $S_{Hmax}$ obtained from this analysis ranges between 39.5 and 43 psi (Fig. 19a). Predictions of wellbore stability based on such values are consistent with drilling experience.

## 10. Estimating $S_{Hmax}$ from breakout rotations

In areas of active faulting, wells penetrate formations where there are localized stress perturbations due to slip on faults. These perturbations are manifest as rotations of breakout (and/or drilling-induced tensile fracture) azimuth along the wellbore as a function of depth. These have been seen in oil and gas wells in several parts of the world. An example of a breakout rotation can be seen in Fig. 20 from the KTB scientific research well in Germany. An ultrasonic televiewer image of a section of the well with a breakout rotation is seen on the left. Through interactive analysis of the shape of the wellbore at various depths, the orientations of the breakouts were determined [36]. The orientation of the breakouts are shown by the dots in the image on the right, along with the orientation of the causative fault (which strikes N50°E and dips 70° to the southeast). Note that with respect to the orientation of the breakouts at 2094 and 2111 m, the breakouts within about 5 m of the fault at 2102 m are rotated clockwise several tens of degrees.

Breakout rotations were first noted in a scientific research well drilled near the San Andreas fault in
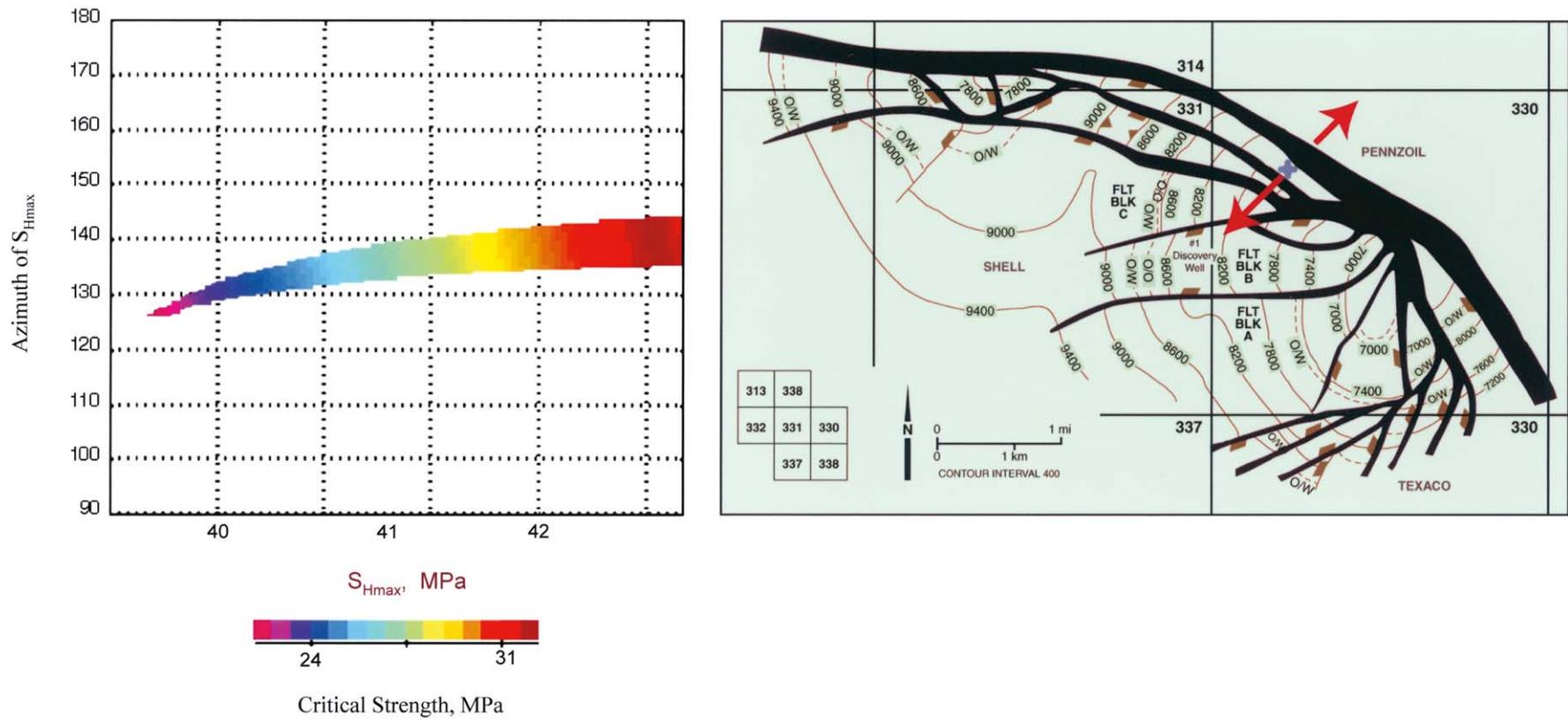
Fig. 19. The figure on the left shows the possible values of $S_{Hmax}$ magnitude and orientation consistent with wellbore breakouts in a deviated well in the Gulf of Mexico. The stress orientation determined in this analysis indicates extension orthogonal to the strike of a major N fault penetrated by the well (after Zoback and Peska [59]).
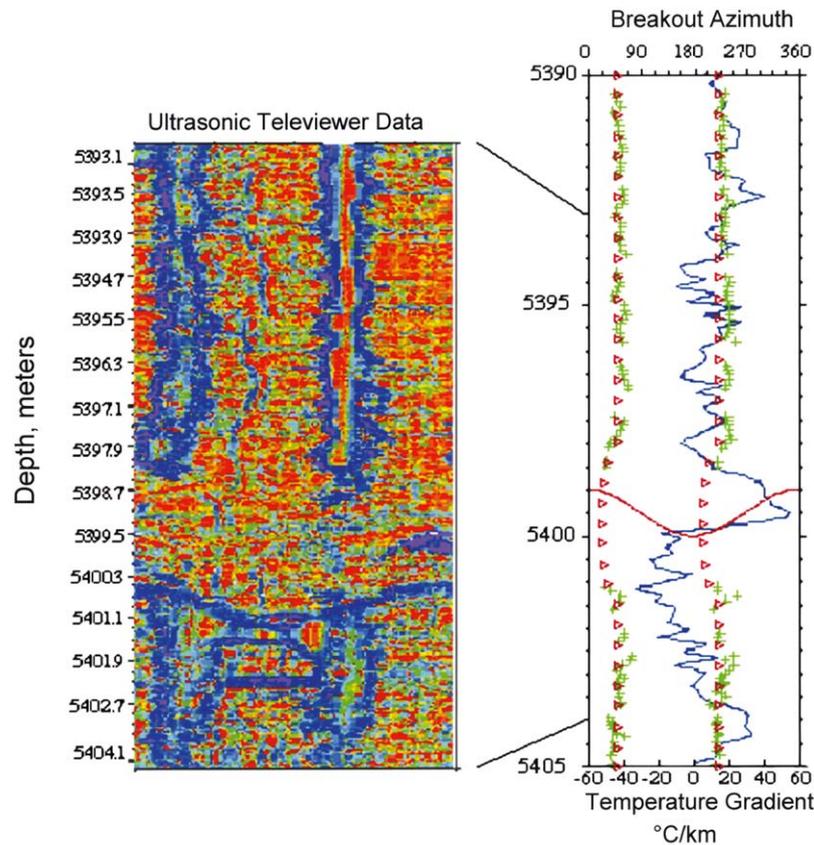
Fig. 20. Rotation of wellbore breakouts near a fault at 5399 m in the KTB borehole that can be modeled as the result of a perturbation of the stress field induced by slip on the fault [61]. This is illustrated on the right (see text).

southern California [60]. In that study, it was shown that slip on active faults was the most likely cause of the breakout rotations. If the different mechanical properties of the faults were the cause of the rotation, the orientation of the breakouts would be perturbed over a much greater length of the wellbores than that observed. Brudy et al. [16] studied breakout and tensile fracture orientation with depth in ultradeep KTB research borehole using wellbore image data and the interactive analysis technique referred to above. They documented the fact that while the average stress orientation to $\sim 8$ km depth was quite consistent, numerous relatively minor perturbations of stress orientation (at various wavelengths) are superimposed on the average orientation due to slip on faults at various scales.

Barton and Zoback [61] used dislocation modeling to replicate the observed breakout rotations in the KTB wellbore at 5.4 km depth (Fig. 20) and showed how modeling could be used to constrain the magnitude of $S_{Hmax}$ based on knowing (i) the magnitudes of $S_{hmin}$ and $S_v$, (ii) the unperturbed orientation of $S_{Hmax}$ and (iii) the strike and dip of the causative fault. Note that the modeling (red triangles on right-hand image) was used to replicate the breakout rotation observed in televiewer data (left image) which are shown by green crosses in the

right image. The breakouts do not form right next to the fault that slipped due to the stress drop on the fault [60]. There is also a temperature gradient anomaly at the position of this fault (blue line in the image on the right) due to fluid flow into the $S_{Hmax}$ borehole along this fault (see [62]). The magnitude of $S_{Hmax}$ determined from modeling the breakout rotation was consistent with the range of values obtained from analysis of drilling-induced tensile fractures and breakouts by Brudy et al. [16] in this well [61].

## 11. Summary and conclusions

Because knowledge of the vertical principal stress and least horizontal principal stress are determinable in a straightforward fashion from density logs, minifracs and LOTs, the task of constraining the full stress tensor at depth often involves determination of the magnitude and orientation of the maximum horizontal stress. In the sections above, we have outlined a number of techniques for determination of the maximum principal stress utilizing observations of compressive and tensile wellbore failure. In numerous studies, these techniques have yielded consistent values at various depths in a
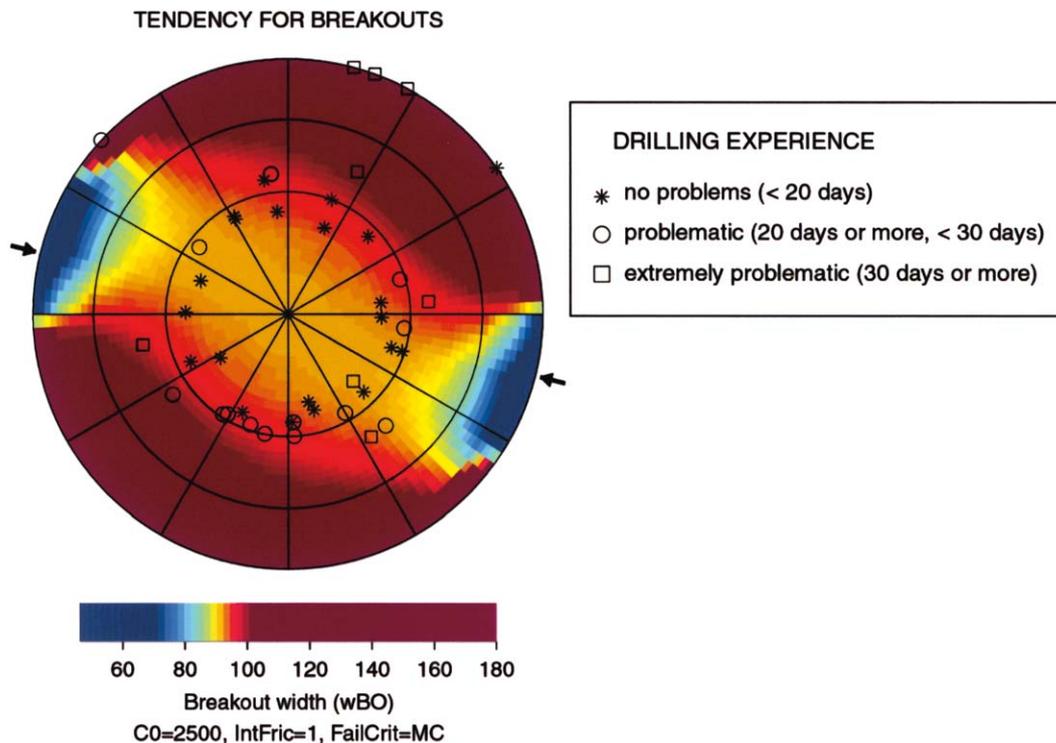
Fig. 21. Drilling experience and drilling direction. The figure shows modeled breakout width in the shales at a depth of 2195 m TVD as a function of drilling direction assuming a mud weight of 10 PPG, and $C_0 = 17.2$ MPa. The total circumference of the wellbore that fails is twice the breakout width. The symbols illustrate the number of days it took to drill the respective well, which is a measure of drilling problems and thus wellbore stability. The color scale ranges from an acceptable breakout width (70°, blue) in which less than half the wellbore circumference fails to an excessive amount failure corresponding to over half the circumference failing (breakout widths over 100°, dark red).

given well and multiple wells in a given field (e.g., [26]). In cases where the wells are drilled in areas of active faulting, the values obtained for $S_{Hmax}$ are consistent with predictions of frictional faulting theory [12,13, 16,53]. In a number of cases where the stress state was determined from a limited number of wells, the stress state successfully predicts compressive and tensile failures in deviated wells drilled subsequently.

Most important from an engineering perspective, predictions of wellbore stability based on stress fields determined using the techniques described above have yielded useful and reliable results. This is illustrated in a case study shown in Fig. 21 where we compare wellbore stability predictions based on the derived stress state to actual drilling experience in a field in a sub-Andean foreland basin in northwestern South America. We have divided the wells in the field into three categories depending on the time needed to drill each well: wells that were drilled in less than 20 days are considered not to be problematic; wells that took more than 20 days are considered to be extremely problematic and those that required more than 30 days are considered to be problematic. In Fig. 20, we compare the predicted failure width and the drilling experience (drilling time) as a function of drilling direction for all wells in the field.

The predicted failure widths displayed in Fig. 21 correlate well with the drilling time. According to our predictions, near-vertical wells at deviations of less than $\sim 30°$ have breakout widths of less than 90° and should therefore pose only minor stability problems. Wells with high deviations drilled towards the NNE/SSW have the largest breakout widths, which explains why wells drilled in this direction were extremely problematic (more than 30 drilling days). The most stable drilling direction is parallel to $S_{Hmax}$ ($\sim 100°/280°$) with a high deviation (near-horizontal). The horizontal well drilled at an azimuth of N55°E would seem to be inconsistent in that it was drilled without problems yet is an unstable direction. However, the mud weight used in this well was higher than the 10 PPG mud weight used in the calculations on which Fig. 21 is based. This decision was made after determination of the orientation and magnitude of principal stresses in the reservoir using the techniques described herein.

### Acknowledgements

measurement techniques described in this paper were developed with financial support from the Stanford Rock and Borehole Geophysics (SRB) consortium.

## References

[1] Willson SM, et al. Drilling in South America: a wellbore stability approach for complex geologic conditions, SPE 53940. In: Sixth LACPEC Conference. Caracas, Venezuela: Society of Petroleum Engineers; 1999.

[2] Zemanek J, et al. Formation evaluation by inspection with the borehole televiewer. Geophysics 1970;35:254–69.

[3] Ekstrom MP, et al. Formation imaging with microelectrical scanning arrays. Log Anal 1987;28:294–306.

[4] Ottesen S, Zheng RH, McCann RC. Wellbore stability assessment using quantitative risk analysis, SPE/IADC 52864. In: SPE/IADC Drilling Conference. Amsterdam, The Netherlands: Society of Petroleum Engineers; 1999.

[5] Moos D, et al. Comprehensive wellbore stability analysis using quantitative risk assessment. In: Aadnoy BS, Ong S, editors. J Pet Sci Eng Spec Issue Wellbore Stability, 2003.

[6] Zoback ML, Zoback MD. State of stress in the conterminous United States. J Geophys Res 1980;85:6113–56.

[7] Zoback MD, Zoback ML. Tectonic stress field of North America and relative plate motions in the geology of North America. In: Slemmons DB, editor. Neotectonics of North America. Boulder CO: Geological Society of America; 1991. p. 339–66.

[8] Zoback ML. First and second order patterns of tectonic stress: the world stress map project. J Geophys Res 1992;97:11703–28.

[9] Lund B, Zoback MD. Orientation and magnitude of in situ stress to 6.5 km depth in the Baltic Shield. Int J Rock Mech Min Sci 1999;36:169–90.

[10] Brudy M. Determination of in-situ stress magnitude, orientation to 9 km depth at the KTB site. In: Geophysics. Karlsruhe, Germany: University of Karlsruhe; 1995.

[11] Anderson EM. The dynamics of faulting and dyke formation with applications to Britain. Edinburgh: Oliver and Boyd; 1951.

[12] Zoback MD, Healy JH. Friction, faulting, and "in situ" stresses. Ann Geophys 1984;2:689–98.

[13] Townend J, Zoback MD. How faulting keeps the crust strong. Geology, 2000;28(5):399–402.

[14] Jaeger JC, Cook NGW. Fundamentals of rock mechanics, ed. Third edition. New York: Chapman & Hall; 1979. p. 28–30.

[15] Byerlee JD. Friction of rock. Pure Appl Geophys 1978;116:615–26.

[16] Brudy M, et al. Estimation of the complete stress tensor to 8 km depth in the KTB scientific drill holes: implications for crustal strength. J Geophys Res 1997;102:18453–75.

[17] Zoback MD, Mastin L, Barton C. In situ stress measurements in deep boreholes using hydraulic fracturing, wellbore breakouts, and Stonely wave polarization. In: Rock stress and rock stress measurements, Proceedings of the Conference 1987. Stockholm, Sweden: Centrek Publications, Lulea.

[18] Moos D, Zoback MD. Utilization of observations of well bore failure to constrain the orientation and magnitude of crustal stresses: application to continental deep sea drilling project and ocean drilling program boreholes. J Geophys Res 1990;95:9305–25.

[19] Baumgärtner J, Zoback MD. Interpretation of hydraulic fracturing pressure - time records using interactive analysis methods. Int J Rock Mech Min Sci Geomech Abstr 1989;26:461–9.

[20] Hubbert MK, Willis DG. Mechanics of hydraulic fracturing. Pet Trans AIME 1957;210:153–63.

[21] Haimson B, Fairhurst C. In situ stress determination at great depth by means of hydraulic fracturing. In: 11th Symposium on Rock Mechanics. Society of Mining Engineers of AIME; London, 1970.

[22] Gaarenstroom L, et al. Overpressures in the Central North Sea: implications for trap integrity and drilling safety. In: Geology of Northwest Europe: Proceedings of the Fourth Conference, 1993.

[23] Hickman SH, Zoback MD. The interpretation of hydraulic fracturing pressure–time data for in-situ stress determination. In: Hydraulic fracturing measurements. Washington, DC: National Academy Press; 1983.

[24] Haimson B, Fairhurst C. Initiation and extension of hydraulic fractures in rocks. Soc Pet Eng J Sept; 1967:310–8.

[25] Nolte KG, Economides MJ. Fracturing diagnosis using pressure analysis. In: Economides MJ, Nolte KG, editors. Reservoir simulation. Englewood Cliffs, NJ: Prentice Hall; 1989.

[26] Wiprut D, et al. Constraining the full stress tensor from observations of drilling-induced tensile fractures and leak-off tests: application to borehole stability and sand production on the Norwegian margin. Int J Rock Mech Min Sci 2000;37:317–36.

[27] Ward CD, Andreassen E. Pressure while drilling data improves reservoir drilling performance—SPE 37588. In: SPE/IADC Drilling Conference, Amsterdam, 1997.

[28] Ward C, Clark R. Anatomy of a balooning borehole using PWD. In: Mitchell A, Grauls D, editors. Overpressures in petroleum exploration. Pau, France: Elf EP-Editions; 1998. p. 213–20.

[29] Ward CD, Clark R. Bore hole ballooning diagnosis with PWD. In: Workshop on Overpressure. Pau, France: Elf EP Editions; 1998.

[30] Ito T, Zoback MD, Peska P. Utilization of mud weights in excess of the least principal stress to stabilize wellbores: Theory and practical examples. Soc Pet Eng Drilling Completions 2001;(16):221–9.

[31] Kirsch G. Die Theorie der Elastizitat und die Bedurfnisse der Festigkeitslehre. VDI Z 1898;42:707.

[32] Aadnoy BS. In situ stress direction from borehole fracture traces. J Pet Sci Eng 1990;4:143–53.

[33] Brudy M, Zoback MD. Drilling-induced tensile wall-fractures: implications for the determination of in-situ stress orientation and magnitude. Int J Rock Mech Min Sci 1999;1999:1999.

[34] Bell JS, Gough DI. Northeast-southwest compressive stress in Alberta: evidence from oil wells. Earth Planet Sci Lett 1979;45:475–82.

[35] Zoback MD, Moos D, Mastin L. Well bore breakouts and in situ stress. J Geophys Res, 1985;90(B7):5523–30.

[36] Barton CA, Tessler L, Zoback MD. Interactive analysis of borehole televiewer data. In: Palaz I, Sengupta SK, editors. Automated pattern analysis in petroleum exploration. New York: Springer-Verlag; 1991.

[37] Castillo D, et al. Trap integrity in the Laminaria high–Nancar trough region, Timor Sea: prediction of fault seal failure using well-constrained stress tensors and fault surfaces interpreted from 3D seismics. APPEA J, 2000;40:1–23.

[38] Wiprut D, Zoback MD. Fault reactivation and fluid flow along a previously dormant normal fault in the northern North Sea. Geology 2000;28:595–8.

[39] Zoback MD, Townend J, Grollimund BR. Steady-state failure equilibrium and deformation of intraplate lithosphere. Int Geol Rev 2002;44:383–401.

[40] Zoback MD, et al. New evidence on the state of stress of the San Andreas fault system. Science 1987;238:1105–11.

[41] Mount VS, Suppe J. State of stress near the San Andreas fault: implications for wrench tectonics. Geology 1987;15:1143–6.

[42] Castillo D, Zoback MD. Systematic stress variations in the southern San Joaquin valley and along the White Wolf fault:

implications for the rupture mechanics of the 1952 ms 7.8 kern county earthquake and contemporary seismicity. J Geophys Res 1995;100(B4):6249–64.

[43] Zoback ML, Zoback MD. Tectonic stress field of the conterminous United States. Geol Soc Am Mem 1989;172:523–39.

[44] Plumb RA, Hickman SH. Stress-induced borehole elongation: a comparison between the four-arm dipmeter and the borehole televiewer in the auburn geothermal well. J Geophys Res 1985;90:5513–21.

[45] Bell JS, Babcock EA. The stress regime of the Western Canadian Basin and implications for hydrocarbon production. Bull Can Pet Geol 1986;34:364–78.

[46] Plumb RA, Cox JW. Stress directions in eastern North America determined to 4.5 km from borehole elongation measurements. J Geophys Res 1987;92:4805–16.

[47] Klein RJ, Barr MV. Regional state of stress in Western Europe. In: Proceedings of the International Symposium on Rock Stress and Rock Stress Measurements. Lulea, Sweden, Stockholm: Centek Publications; 1986. 694pp.

[48] Stephens G, Voight B. Hydraulic fracturing theory for conditions of thermal stress. Int J Rock Mech Min Sci 1982;19:279–84.

[49] Ritchie RH, Sakakura AY. Asymptotic expansions of solutions of the heat conduction equation in internally bounded cylindrical geometry. J Appl Phys 1956;27:1453–9.

[50] Zheng Z, Kemeny J, Cook NG. Analysis of borehole breakouts. J Geophys Res 1989;94(B6):7171–82.

[51] Haimson BC, Herrick CG. Borehole breakouts and in situ stress. In: 12th Annual Energy-Sources Technology Conference and Exhibition, Houston, TX, 1989.

[52] Barton CA, Zoback MD, Burns KL. In-situ stress orientation and magnitude at the Fenton geothermal site, New Mexico, determined from wellbore breakouts. Geophys Res Lett, 1988; 15(5):467–70.

[53] Zoback MD, Healy JH. In situ stress measurements to 3.5 km depth in the Cajon Pass Scientific Research Borehole: implications for the mechanics of crustal faulting. J Geophys Res 1992;97:5039–57.

[54] Peska P, Zoback MD. Compressive and tensile failure of inclined wellbores and determination of in situ stress and rock strength. J Geophys Res, 1995;100(B7):12791–811.

[55] Peska P, Zoback MD. Stress and failure of inclined boreholes SFIB v2.0: Stanford Rock Physics and Borehole Geophysics Annual Report 57, Paper H3, Department of Geophysics, Stanford University, 1996.

[56] Brudy M, Zoback MD. Compressive and tensile failure of boreholes arbitrarily inclined to principal stress axes: application to the KTB boreholes, Germany. Int J Rock Mech Min Sci 1993;30:1035–8.

[57] Zoback MD, et al. Strength of continental crust and the transmission of plate-driving forces. Nature, 1993;365:633–5.

[58] Baumgärtner J, Carvalho J, McLennan J. Fracturing deviated boreholes: an experimental approach. In: Rock at great depth, Proceedings of the ISRM-SPE International Symposium. Elf Aquitaine, Pau: A.A. Balkema; 1989.

[59] Zoback MD, Peska P. In-situ stress and rock strength in the GBRN/DOE Pathfinder well South Eugene Island, Gulf of Mexico, July 1995. J Pet Technol 1995:582–5.

[60] Shamir G, Zoback MD. Stress orientation profile to 3.5 km depth near the San Andreas Fault at Cajon Pass California. J Geophys Res 1992;97:5059–80.

[61] Barton CA, Zoback MD. Stress perturbations associated with active faults penetrated by boreholes: possible evidence for near-complete stress drop and a new technique for stress magnitude measurements. J Geophys Res 1994;99:9373–90.

[62] Barton CA, Zoback MD, Moos D. Fluid flow along potentially active faults in crystalline rock. Geology, 1995;23:683–6.